https://doi.org/10.5194/egusphere-2026-3221
Preprint. Discussion started: 7 August 2026

Concurrent assimilation of methane fluxes and concentrations with a 4D LETKF for Germany in 2021 based on ICON–ART

Niklas Becker[1], Valentin Bruch[1], Thomas Rösch[1], Niels H. Keil[1], Martin J. Steil[1], Diego Jiménez de la Cuesta Otero[1], Beatrice Ellerhoff[1], Roland Potthast[1], and Andrea K. Kaiser-Weiss[1]

[1]Deutscher Wetterdienst, Frankfurter Str. 135, 63067 Offenbach

Correspondence: Niklas Becker (niklas.becker@dwd.de) and Andrea K. Kaiser-Weiss (andrea.kaiser-weiss@dwd.de)

Abstract. Greenhouse gas (GHG) emission quantification is crucial for assessing and mitigating climate change. We present a data assimilation system that can adjust methane concentrations and fluxes concurrently, by augmenting the state vector. We rely on the high resolution numerical weather prediction model ICON to simulate the atmospheric transport of GHG and the associated uncertainties, and assimilate to GHG observations of the Integrated Carbon Observation System (ICOS) station network with a 4D Local Ensemble Transform Kalman Filter (LETKF) system. We use two different approaches to adjust the emissions, one with a perturbed field, the other with a split into emission categories. The results confirm significantly higher methane emissions in Germany compared to the reported national inventory, as well as higher emissions in the BeNeLux region. The 4D LETKF contributes to a comprehensive system to validate national greenhouse gas emission reporting, adding the advantage of spatial flexibility for flux attribution and paving the way for near real time applications.

1 Introduction

To mitigate anthropogenic climate change, the reduction of greenhouse gas (GHG) emissions is critical. Methane (CH_4) is the second most important anthropogenic GHG, and its reduction plays an essential role, especially in the near term (Shindell et al., 2012; Arias et al., 2021). This has led to the "Global Methane pledge", with the collective goal to reduce emissions by 2030 by at least 30% compared to 2020 (European Commission, 2021).

To assess the effectiveness of policies aimed at emission reduction, UNFCCC compliant national inventories (NIRs) are implemented by governments around the world. NIRs are compiled with socioeconomic statistics, activity data and emission factors, referred to as *bottom-up* approach here. As transparency spurs climate action (Stern, 2025), *top-down* strategies are applied by estimating GHG emissions from atmospheric measurements. This approach is complementary to bottom-up inventories and recommended by the 2019 Refinement of the 2006 IPCC Guidelines for National Greenhouse Gas Inventories (IPCC et al., 2019). Recently, top-down methods are starting to be implemented by the scientific community for the purpose of national GHG flux estimation, but challenges remain as pointed out by Ganesan and Manning (2025).

In these inverse modeling problems, GHG observations are linked to emissions with the help of atmospheric transport models (ATMs). The ATMs model the transport of the GHGs from the emission source to the observation site. Solving the inverse problem is usually based on minimizing a Bayesian cost function, given a set of prior assumptions – such as the NIRs

https://doi.org/10.5194/egusphere-2026-3221
Preprint. Discussion started: 7 August 2026

– and the involved uncertainties. The inversion techniques include synthesis inversion (Kaminski et al., 2001; Bruch et al., 2025a), Kalman filter (Nakamura and Potthast, 2015), 4D variational methods (Le Dimet and Talagrand, 1986; Meirink et al., 2008; Bergamaschi et al., 2013), and ensemble Kalman filter methods (Evensen, 1994; Chen et al., 2019).

These have been widely used for some GHGs such as carbon dioxide (Basu et al., 2020), halocarbons (Stohl et al., 2009), nitrous oxide (Ganesan et al., 2015) and CH_4, on different scales, e.g., for the UK in Manning et al. (2011), for Switzerland in Henne et al. (2016), for Europe in Petrescu et al. (2023); Steiner et al. (2024b) and globally in Deng et al. (2022); Petrescu et al. (2024); Estrada et al. (2024).

One of the largest uncertainties in the top-down approach comes from the transport modeling of the trace gases (Enting, 1993; Engelen et al., 2002; Munassar et al., 2023). Uncertainties arise in the numerical treatment of the transport problem, as well as the initial and boundary conditions of the meteorology and trace gases (Chen et al., 2019). These uncertainties can be reduced using a high resolution (Gerbig et al., 2008), and approximated using ensemble methods (Steiner et al., 2024a; Bruch et al., 2025a).

To assess the uncertainties holistically, we perform an ensemble based assimilation for the concentrations and emissions at the same time. This has been used in aerosol modeling e.g. by Miyazaki et al. (2012); Peng et al. (2017), and for CH_4 in an observation system simulation experiment by Bisht et al. (2023).

Here, we explore the suitability of a local ensemble transform Kalman filter (LETKF) for national GHG emission estimates for Germany, by adjusting both concentrations and emissions of CH_4 during the assimilation. We use two different approaches for the emission estimation: We adjust the emissions based on a perturbed field approach, where we perturb the emission field with gaussian random fields, which have a spatial correlation structure. Alternatively, we sort the emission field into categories, according to regions and economic sectors, and scale these categories. We show that both approaches produce similar results, also comparable with synthesis inversion results from Bruch et al. (2025a, b, 2026). We compare our results with the method presented in these publications, referred to as *B25*.

We rely on the numerical weather prediction (NWP) system of the German Meteorological Service (DWD), i.e., Eulerian modeling of atmospheric transport for three reasons. Firstly, our Eulerian approach allows a flexible use of numerous in-situ and remote sensing data, which would become computationally prohibitive for Lagrangian approaches in case of large amounts of observations, e.g., with satellite data. Secondly, by benefiting from high resolution NWP quality, we reduce the transport error and gain some characteristics of the latter by means of ensembles. Thirdly, we can reap technical benefits of using a high performance NWP data assimilation system as testbed for inversion methods. The two approaches presented here complement each other: While the category split allows defining areas of interest (like countries) and therefore can be tailored to policymakers' needs, the emission state space is limited by the category selection. The perturbed field approach is more flexible in its state space, and can help inform where the category split is insufficient.

The structure of this paper is as follows: In Section 2, we explain the technical setup of our modular system and the data flow for the data assimilation cycle. In Section 3, we present the concurrent assimilation and the two emission adjustment approaches: perturbed field and category split. In Section 4, we explore the method using a sample month of 2021, and in

https://doi.org/10.5194/egusphere-2026-3221
Preprint. Discussion started: 7 August 2026

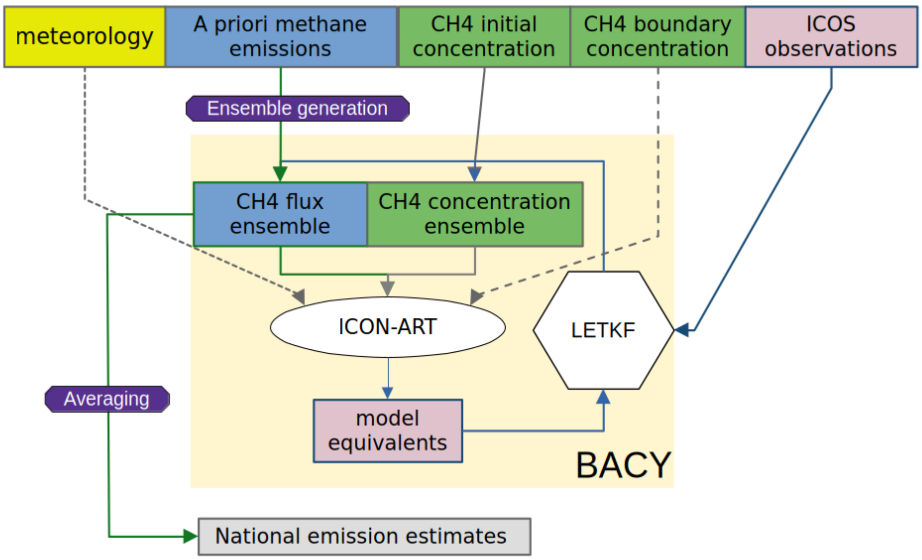

Figure 1. The technical setup and data flow of the data assimilation cycle.

Section 5, we present the results for the whole year and discuss the capabilities and limitations of the method, concluding in Section 6.

2 Technical Setup

An overview of the technical setup and data flow is shown in Figure 1. The components are described in detail in the following.

2.1 Meteorology

The atmospheric transport is modeled with the numerical weather prediction (NWP) Icosahedral Nonhydrostatic model (ICON) version icon-2024.10-dwd-2.1 (Zängl et al., 2015) along with its aerosol and reactive trace gas module ART (Rieger et al., 2015; Schröter et al., 2018). The model is run in the limited area mode with a domain covering most of the European continent (34° N to 70° N, 21° W to 59° E). The domain has a horizontal resolution of $6.5\,\mathrm{km}$ (ICON grid R3B8) and $N_{lev} = 74$ vertical levels up to a maximal height of $22.77\,\mathrm{km}$. The domain is made up of $N_{grid} \sim 5 \cdot 10^5$ grid cells and is shown in Figure 2. We use hyperparameters similar to the operational settings of the NWP at the DWD. [1]

For the meteorological input data we use the reanalysis ICON-DREAM (Valmassoi et al., 2025) with 20 ensemble members. We do not assimilate the meteorological data, but reinitialize the simulation every day at 00:00 UTC, such that the model meteorology remains aligned with the reanalysis.

[1] The most notable difference is the namelist setting transport_nml/beta_fct=1, which prevents overshoot in the flux limiters and increases diffusivity.

https://doi.org/10.5194/egusphere-2026-3221
Preprint. Discussion started: 7 August 2026

Shortname	Short description	Version
GRETA	Anthropogenic German emissions from UBA	Submission 2025, GRETA 1.6 (Feigenspan and Wernicke, 2025)
reeks2022def	Anthropogenic Dutch emissions from RIVM	2022def (Witt, 2025)
CAMS-REG-ANT	Anthropogenic European emission	v8.1 (Kuenen et al., 2022, 2021a, b)
inland waters global	Natural emissions from inland waters in Europe	(Rocher-Ros et al., 2023)
oceans	Natural emissions from oceans	(Weber et al., 2019)
WetCHARTs	Natural emissions from wetlands in Europe	v1.3.3 (Bloom et al., 2024)

Table 1. The datasets used to construct the a priori fluxes in the domain.

2.2 A priori CH_4 fluxes

The methane emission data for Germany, the Gridding Emission Tool for ArcGIS (GRETA) were provided by the Umweltbundesamt and Thünen Institut, based on the national greenhouse gas reporting to the UNFCCC (UBA, 2025). For the Netherlands, we use a dataset provided by the dutch National Institute for Public Health and the Environment (RIVM) (van der Net et al., 2025). Outside of these countries, anthropogenic fluxes were taken from the CAMS-REG-ANT dataset available at the ECCAD database (Kuenen et al., 2021a). The complete list of datasets used is provided in table Table 1. We assume constant fluxes throughout a month.

The surface CH_4 emissions are introduced into ICON-ART with the online emissions module (OEM) module (Jähn et al., 2020; Steiner et al., 2024a).

2.3 CH_4 initial and boundary concentrations

To initialize our model, and to provide the lateral boundary data that enters the domain, we use the Copernicus Atmospheric Monitoring Service (CAMS) global inversion-optimized dataset (version: v24r1, time aggregation: instantaneous, and input observations: surface) (Segers and Houweling, 2020). This dataset has a horizontal spatial resolution of $1^\circ \times 1^\circ$ and is interpolated onto our model grid.

2.4 ICOS observations

We employ the in-situ CH_4 concentration observations of the European Obspack (ICOS RI et al., 2024) provided by the ICOS carbon portal (ICOS RI, 2024). For tower observations, we use the highest available sampling height, which is representative of a larger area (Storm et al., 2023). The stations that were used for the assimilation in 2021 are shown in Figure 2.

We use the observations at 3:00 UTC of mountain stations (those above 1.5 km above sea level), and observations at 12:00, 15:00 UTC of non-mountain stations for the assimilation[2]. This is typical in atmospheric inverse modeling as there are difficulties in representing nocturnal boundary layers in NWP models (Steiner et al., 2024a).

[2]The observations in the dataset are given at half hour timestamps, representing the average over the hour. For the observations at the full hour we interpolate the neighboring two timestamps, e.g. for 15:00 we take the average between 14:30 and 15:30.

https://doi.org/10.5194/egusphere-2026-3221
Preprint. Discussion started: 7 August 2026

2.5 BACY

The Basic Cycling (BACY) environment manages the cycling from one assimilation step to the next. The ICON-ART model simulates the concentration fields according to the fluxes, the meteorology, and the boundary concentrations. At the location and times of observations the so-called "model equivalents" are written out. The LETKF uses the model equivalents together with the observations to modify the concentration ensemble as well as the flux ensemble such as to match the observations closer. The resulting analysis of the LETKF, i.e. the concentration ensemble and the flux ensemble, serve as input for the next time step. This cycling is run over, e.g., a month, and the resulting flux analysis fields are postprocessed to yield the desired top-down national emission estimates.

3 Data Assimilation

The data assimilation is performed with the Localized Ensemble Transform Kalman Filter (LETKF) method (Hunt et al., 2007). We present the method following Schraff et al. (2016).

3.1 LETKF

At a given time t, we have an estimate of the system state through the ensemble $\{x^{b(i)} : i = 1,..,\ell\}$. Here, the system generally refers to the combination of the concentrations on the grid $x^{b(i),c}$, and a vector representing the emissions $x^{b(i),e}$. The exact construction approaches of this background vector are explained in the sections Sections 3.2 to 3.4.

Given some observations y^0, we want to find the best fit of the system state given by the cost function

$$J(x) = \|x - \bar{x}^b\|^2_{(\mathbf{P}^b)^{-1}} + \|y^0 - H(x)\|^2_{\mathbf{R}^{-1}}\,. \tag{1}$$

Here, $\bar{x}^b$ is the mean of the background ensemble, $\mathbf{P}^b$ the background error covariance matrix, $\mathbf{R}$ the observation error covariance matrix, and $H(x)$ the observation operator. We use the notation $\|x\|^2_{\mathbf{M}} = x^T\mathbf{M}x$ for the norm of x weighted by a positive definite matrix $\mathbf{M}$.

In the LETKF, the background error covariance matrix is given by the ensemble covariance

$$\mathbf{P}^b = (\ell - 1)^{-1}\mathbf{X}^b(\mathbf{X}^b)^T, \tag{2}$$

where the columns of the matrix $\mathbf{X}^b$ are the deviations of the ensemble members to the ensemble mean $x^{b(i)} - \bar{x}^b$.

The observation operator $H(x)$ is assumed to be linear such that

$$H(\bar{x}^b + \mathbf{X}^b w) = \bar{y}^b + \mathbf{Y}^b w\,. \tag{3}$$

Here, $\bar{y}^b = \overline{H(x^{b(i)})}$ and $\mathbf{Y}^b$ is the ensemble perturbation matrix in observation space.

We aim to find the system state x that minimizes the cost function Equation (1). Assuming the solution lies in the span of the ensemble, we can write $x = \bar{x}^b + \mathbf{X}^b w$ and transform the cost function to

$$J(w) = (\ell - 1)\|w\|^2 + \|y^0 - \bar{y}^b - \mathbf{Y}^b w\|^2_{\mathbf{R}^{-1}}\,, \tag{4}$$

https://doi.org/10.5194/egusphere-2026-3221
Preprint. Discussion started: 7 August 2026

where $w \in \mathbb{R}^\ell$ is a vector in ensemble space, which is much lower-dimensional than the state space.

This transformed cost function can be explicitly minimized to obtain the analysis by

$$\bar{w}^a = \tilde{\mathbf{P}}^a (\mathbf{Y}^b)^T \mathbf{R}^{-1} (y^0 - \bar{y}^b), \tag{5}$$

$$\tilde{\mathbf{P}}^a = [(\ell - 1)\mathbf{I} + (\mathbf{Y}^b)^T \mathbf{R}^{-1} \mathbf{Y}^b]^{-1}, \tag{6}$$

with the analysis mean $\bar{w}^a$ in ensemble space, and the analysis error estimation $\tilde{\mathbf{P}}^a$. The analysis ensemble perturbations are given by the columns of

$$\mathbf{W}^a = [(\ell - 1)\tilde{\mathbf{P}}^a]^{1/2} \tag{7}$$

such that the analysis ensemble member in state space are given by

$$x^{a(i)} = \bar{x}^b + \mathbf{X}^b (\bar{w}^a + \mathbf{W}^{a(i)}). \tag{8}$$

Therefore, the analysis ensemble members are constructed from a point-wise linear combination of the background ensemble members, and represent the best guess given the combination of background and observations.

3.1.1 Localization

An important part of the LETKF is the localization. To avoid spurious large scale correlations due to the finite ensemble size, a localization is introduced through the observation error covariance matrix $\mathbf{R}$. This matrix can be constructed point-wise. The matrix is chosen to be diagonal and constructed for each point with position p_k such that

$$\mathbf{R}_{jj}^{-1} = \frac{\mathrm{GC}(\mathrm{vdist}(p_k, p_j), c_v) \cdot \mathrm{GC}(\mathrm{hdist}(p_k, p_j), c_h)}{\sigma_j^2}, \tag{9}$$

where σ_j represents the observation uncertainty, p_j the position of the observation, and vdist, hdist the vertical and horizontal distance between the points, respectively.

The localization is achieved with the help of the Gaspari-Cohn (GC) function (Gaspari and Cohn, 1999), which resembles a Gaussian but has compact support. We employ a vertical c_v and horizontal c_h scale parameter, such that the GC function is zero at twice the scale parameter. Therefore, the localization is a cylinder in physical space, and observations outside this cylinder have no influence on the model point central to the cylinder.

3.1.2 Uncertainty Inflation

The state vector can be a combination of the CH_4 concentrations in the model grid at the assimilation time $x^{b(i),c}$, as well as the emissions that were active in the model $x^{b(i),e}$. We can apply a covariance inflation factor to each component individually to scale the uncertainties component-wise

$$\mathbf{X}^b = \left[\begin{pmatrix} \sqrt{\rho_c}(x^{b(i),c} - \bar{x}^{b,c}) \\ \sqrt{\rho_e}(x^{b(i),e} - \bar{x}^{b,e}) \end{pmatrix} \right]_i. \tag{10}$$

https://doi.org/10.5194/egusphere-2026-3221
Preprint. Discussion started: 7 August 2026

where ρ_c and ρ_e are the inflation factors, and the subscript i refers to the columns of the matrix.

Multiplicative covariance inflation is not critical for gases that move in and out of the limited domain. It is more tricky for the emissions, which are stationary. Here, the inflation factor would need to be fine-tuned to avoid either preemptive convergence or divergence of the uncertainty. To circumvent fine tuning, we introduce a minimal point-wise standard deviation σ^e_{min} for the emission state vector $x^{b,e}$ after each assimilation step.

3.1.3 Observation Treatment

We assimilate daily at 15:00 UTC model time. The observation vector y^0 consists of the observations at 3:00 UTC, 12:00 UTC, and 15:00 UTC. In this sense, we employ a 4D-LETKF. We assume a minimal model-observation error of $\sigma_{\text{obs}} = 5\,\text{ppb}$, and quadratically add the temporal standard deviation of the hourly ICOS observations to obtain the observation uncertainty σ_j.

The model equivalent is calculated at the respective observation times with the help of the ICON meteogram files (Prill et al., 2024), which save the model data in $15\,\text{min}$ intervals around the observation sites during the run. We select an hourly window, average the respective 5 meteograms, and interpolate spatially to the observation sites. The horizontal interpolation is with the inverse distance method to the 6 nearest cells, the vertical interpolation linear to the position halfway between height above sea level and model ground for mountain stations, and to height above model ground for the other stations. This is done because the smooth model topography typically underestimates the actual altitude of the mountain sites (Steiner et al., 2024a).

3.1.4 Cycling

The resulting analysis concentrations and emissions are then used as the starting point for the next cycle step. We use an ensemble size of $\ell = 100$ for the emission assimilations. Since we have a meteorological ensemble of size twenty, we utilize five different CH_4 tracers per meteorological ensemble member in ICON–ART. Therefore, five ensemble members each share the same meteorology and transport.

3.2 Perturbed Field Approach

To adjust emissions with the assimilation, the LETKF method needs an ensemble of emissions. We can construct an ensemble of point-wise perturbations on the model grid. First, we create a field of total emissions $e \in \mathbb{R}^{N_{grid}}$ inside our domain by summing up all the different emission sources. Then, we multiply with Gaussian random numbers varying per grid cell. To reduce the effective degrees of freedom and assume spatial correlations, we employ Gaussian random fields for these multiplicative factors.

Here, a Gaussian random field is a field of 2D points $p_n \in \mathbb{R}^2$ with a Gaussian random variable X_n at each point. If we assume the field to be isotropic and homogeneous, the random variables $X \sim \mathcal{N}(\mu, \mathbf{\Sigma})$ have a correlation that depends only on their distance $\Sigma_{nm} \sim C(|p_n - p_m|)$. In this case, we can define the *power spectrum* as the Fourier transform of the correlation function

$$P(k) = \int C(p) e^{-ikp} dp. \tag{11}$$

https://doi.org/10.5194/egusphere-2026-3221
Preprint. Discussion started: 7 August 2026

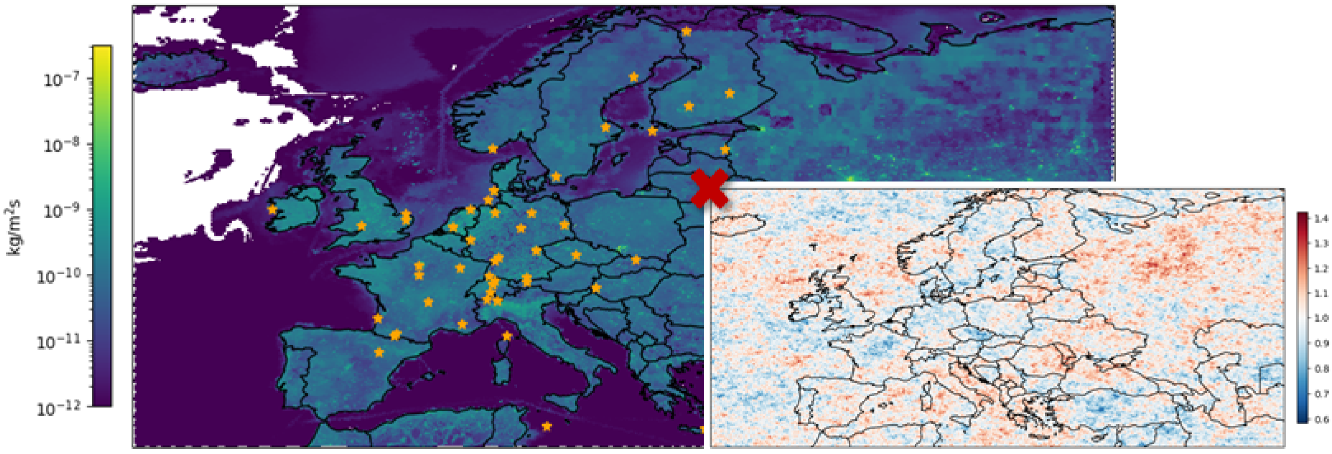

Figure 2. The average total emission prior for 2021 in the model domain, multiplied by a realization of a scale-free Gaussian random field with power law index $\alpha = 0.4$. The orange stars show the location of the observation sites of the European Obspack that were used (partially covered is the station FKL in Crete).

A *scale-free* Gaussian random field is a field, where the power spectrum is given by a power law $P(k) \sim k^{-\alpha}$. These have correlations on all scales and are self-similar over different orders of magnitude. We show an example with $\alpha = 0.4$ in Figure 2.

We employ an ensemble of these scale-free Gaussian fields $X^{(i)}$ with mean $\mu = 1$, ensemble size ℓ, power-law index α, and point-wise standard deviation σ_p. Then, we multiply each with the total emissions per gridpoint, such that we get an ensemble of perturbed gridded total emissions. The emission state vector of the previous section is then $x_n^{b(i),e} = X_n^{(i)} e_n$. The choice of α will be discussed in Section 4.2.1. The total emissions are approximately conserved due to the mean being $\mu = 1$.

This approach assumes the uncertainties in the emission field to be spatially correlated, with the given correlation structure, e.g. closeby points are more strongly correlated. In this, it ignores the source type, borders and other policy induced large scale correlations.

3.3 Category Split Approach

Alternatively to the perturbed field approach, we can utilize the category split similar to the one introduced in *B25*. We collect emissions by region and anthropogenic sector into categories, which are shown in Figure 3. In comparison to *B25*, we have refined the split into smaller regions.

Inside Germany, we generally follow the administrative borders of the states and consider the sectors agriculture (GNFR[3] sectors K+L) (termed *.KL*), natural fluxes + LULUCF (*.N*), and the rest (which includes, e.g., public power and waste) (*.nKLN*). Outside of Germany, we do not differentiate anthropogenic emission sectors, except in the Netherlands. There, agricultural emissions have a strong influence on the CH_4 concentration in Germany due to its proximity. Natural + LULUCF fluxes are a separate category in Germany, Scandinavia, and the north-eastern part of the domain, due to their strength in these areas.

[3] Gridded Nomenclature For Reporting

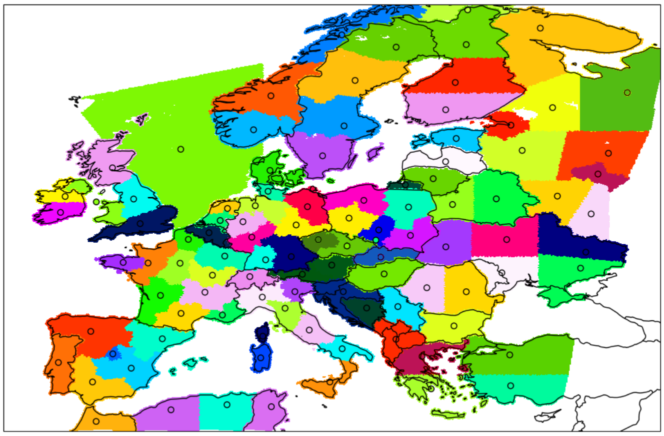

Figure 3. The different regions for the category split in the model domain. The points represent the localization of the categories. The categories that are outside the localization radii of all observation sites are not assimilated.

All other categories are total fluxes from the corresponding regions, which roughly follow borders where feasible. The further away from Germany, the less granular these become, generally.

We end up with $N_{cat} = 142$ categories covering the model domain. We assign them a center through emission weighted averaging of the gridpoints making up the category. This is used for the localization of the LETKF. The centers are shown in Figure 3.

To obtain an ensemble for the LETKF, we draw uncorrelated Gaussian random numbers for the scale factors of these categories $\lambda^{(i)} \in \mathbb{R}^{N_{cat}}$, with mean 1, and standard deviation σ_s. The emission state vector is then given by these scale factors $x^{b(i),e} = \lambda^{(i)}$.

On a technical level, in contrast to *B25*, we do not introduce these categories as different tracers into ICON-ART. Instead, we sum up all contributions of the categories with their associated scale factors and only introduce this sum as the source for the CH_4 tracer into ICON–ART. The scale factors of the categories will then be assimilated through their correlation with the observations only.

This approach assumes the spatial distributions within the emission categories to be correct and the uncertainty to be in their magnitude.

3.4 Simulation Setup

We simulate each month individually in the year 2021. For each month, we run four simulations:

(i) A free forecast without any assimilation

(ii) Adjusting only the CH_4 concentrations with the state vector $x^{b(i)} = x^{b(i),c}$, with $x^{b(i),c} \in \mathbb{R}^{N_{grid} \cdot N_{lev}}$.

https://doi.org/10.5194/egusphere-2026-3221
Preprint. Discussion started: 7 August 2026

(iii) Adjusting the concentrations and the perturbed emission field with the state vector $x^{b(i)} = \begin{pmatrix} x^{b(i),c} \\ x^{b(i),e} \end{pmatrix}$, with $x^{b(i),e} \in \mathbb{R}^{N_{grid}}$.

(iv) Adjusting the concentrations and the category split with the state vector $x^{b(i)} = \begin{pmatrix} x^{b(i),c} \\ x^{b(i),e} \end{pmatrix}$, with $x^{b(i),e} \in \mathbb{R}^{N_{cat}}$.

We use these different simulations to contrast and compare the methods. We start the simulation on the 25$^{\text{th}}$ of the previous month and assimilate daily at 15:00 UTC.

3.5 Emission Posteriors

For the simulations (iii) and (iv), the assimilation cycle produces a best estimate of the emission field each day. To obtain the emission posterior for the whole month, the uncertainty weighted temporal average of the emission field is taken, starting from the first of the month. Thus, we allow for a few days of ‘burn-in‘ of the assimilation. The posterior uncertainty is calculated with the incremental weighted algorithm (West, 1979) to obtain the variance over the time and ensemble dimensions. The country posteriors are obtained by first calculating the daily mean and standard deviation of the emission posterior, and then taking the temporal average. For (iv), we average the scale factors in the same manner.

For the simulation (iii) with the perturbed field approach, we can introduce a sector attribution in a ‘post-hoc‘ manner. We assume the sector decomposition of the prior to be correct gridpoint-wise, and use the fraction of the posterior over the prior point-wise to scale this decomposition. This approach is used e.g. in Wecht et al. (2014); Estrada et al. (2024).

4 Method Application

In this section we explore the two approaches to adjust the emissions introduced in the previous section. We start with a sample month to discuss their properties and then explain the hyperparameter choices.

4.1 Sample Month

To explore the approaches in detail, we look at September 2021. We contrast and compare the four simulations introduced in Section 3.4.

The standard hyperparameters we chose are listed in Table 2.

4.1.1 Perturbed Field Approach Application

To begin, we show an example assimilation step for September 1st in Figure 4. The analysis concentration increment can be converted into the analysis mass increment and summed over the vertical levels to obtain it gridpoint-wise. As seen in the figure, the mass and emission updates do not necessarily spatially align, which indicates that the method can, in principle,

https://doi.org/10.5194/egusphere-2026-3221
Preprint. Discussion started: 7 August 2026

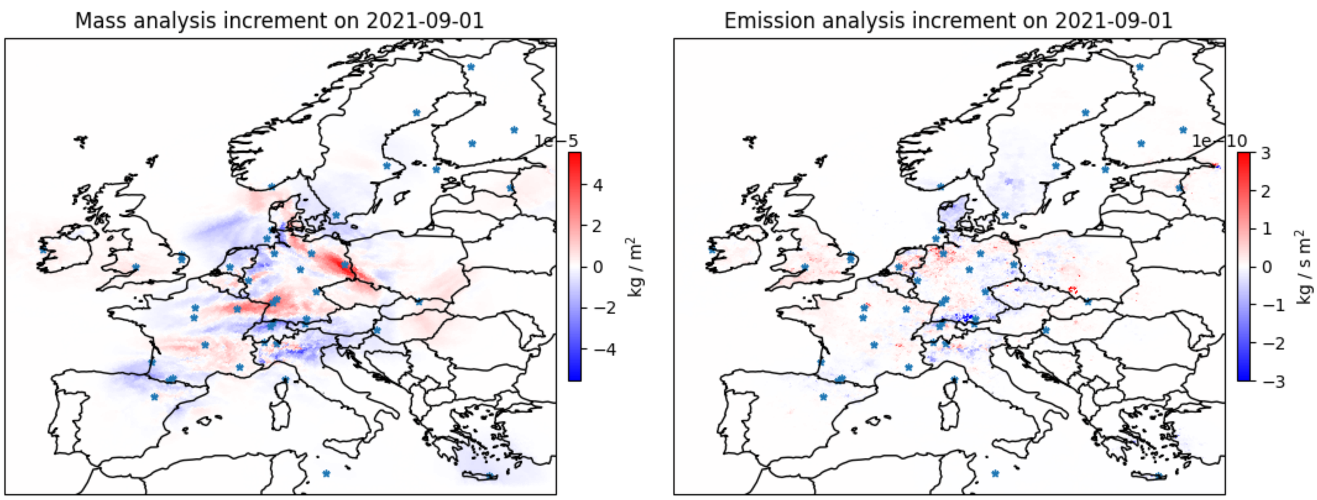

Figure 4. The analysis increment of the (iii) perturbed field approach assimilation step for September 1st, 2021. **Left**: The analysis mass increment summed over the height levels after the concentration adjustment. **Right**: The analysis emission increment. The blue stars represent the observation sites used in this assimilation step. The two increments are spatially distinct.

differentiate between concentration and emission updates. The scale-free gaussian random field structure can be seen in the emission analysis increment, subject to the localization around the observation sites.

Table 2. Table of hyper-parameters with description and default values used in this analysis.

Name	Description	Simulation	Value
ℓ	Number of ensemble members	(i),(ii)	20
ℓ	Number of ensemble members	(iii),(iv)	100
c_h	Horizontal GC localization length	(ii),(iii),(iv)	300 km
c_v	Vertical GC localization length	(ii),(iii),(iv)	1500 m
σ_{obs}	Minimal observation uncertainty	(ii),(iii),(iv)	5 ppb
ρ_c	Concentration inflation factor	(ii),(iii),(iv)	1.8
α	Gaussian random field power law index	(iii)	0.5
ρ_p	Emission perturbation inflation factor	(iii)	1.005
σ_p	Initial point-wise relative standard deviation	(iii)	0.5
σ_p^{min}	Minimal point-wise ensemble relative standard deviation	(iii)	0.2
ρ_s	Emission perturbation inflation factor	(iv)	1.02
σ_s	Initial categorical standard deviation	(iv)	0.5
σ_s^{min}	Minimal ensemble standard deviation	(iv)	0.2

https://doi.org/10.5194/egusphere-2026-3221
Preprint. Discussion started: 7 August 2026

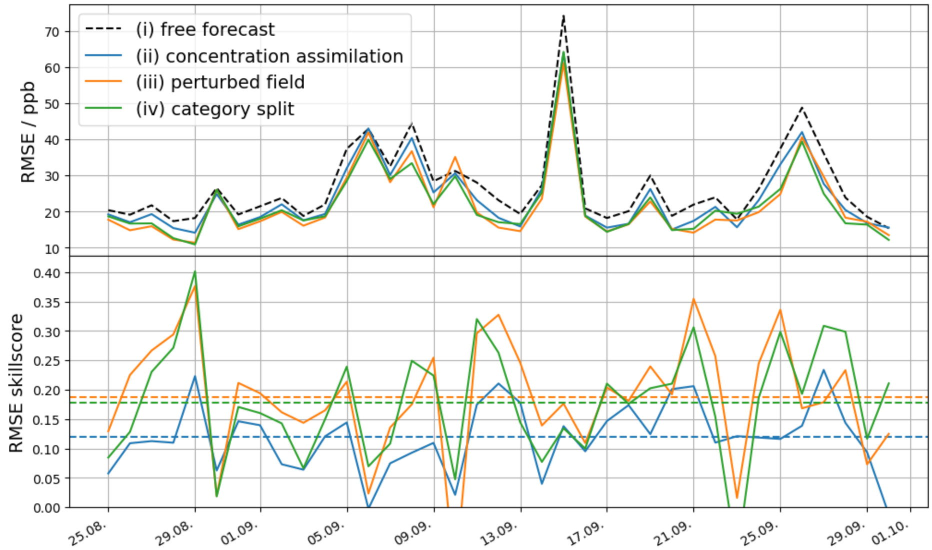

Figure 5. Top: The daily RMSE for all observation sites for the four simulations. **Bottom**: The associated skillscore for the three simulations (ii),(iii),(iv) compared to (i), which represents the % decrease in RMSE. The dashed lines show the average. The concurrent assimilation reduces the RMSE.

Through comparison with the observations, the daily root mean square error (RMSE) can be calculated for each simulation (i)-(iv). Here, we use all hourly observations between 22:00–03:00 UTC for mountain stations, and 11:00–16:00 UTC for all others (including the hour after the assimilation). This is shown in Figure 5, along with the RMSE skillscore, which shows the improvement of (ii)-(iv) in comparison to (i). On average, the concentration adjustment (ii) reduces the RMSE by about $\sim 12\%$, while the concurrent adjustment (iii) has a $\sim 19\%$ improvement. While there are individual days where the concurrent adjustment performs worse, it has a better performance on average.

The evolution of the total emissions in Germany throughout the month is shown in Figure 6. There is an initial increase during the burn-in period, which has a turnaround and later flattens out, while the uncertainty decreases. The dashed line indicates the mean starting from the first of the month. We can see here that the emissions seem to stay close to the mean starting from the middle of the month, but we include the whole month for the posterior estimation. If the emissions were truly constant throughout the month, we could wait for apparent convergence, or implement a convergence criterion. But this is not necessarily a given, and to anticipate temporal changes, we try to include the whole month as a deliberate choice.

The spatial distribution of the emission posterior – or rather, the difference from prior to posterior – is shown in Figure 7. We can see increases throughout Germany, especially in the Northwest, along with increases in the BeNeLux region. Here, also the relative standard deviation of the posterior decreased, compared to the prior. The change in relative standard deviation is located around the observation sites. Some regions show an increase, most notably the Pyrenees and parts of the Alps, as mountainous regions can be difficult to model. Other parts include the North Sea, where due to low posterior emissions, even

https://doi.org/10.5194/egusphere-2026-3221
Preprint. Discussion started: 7 August 2026

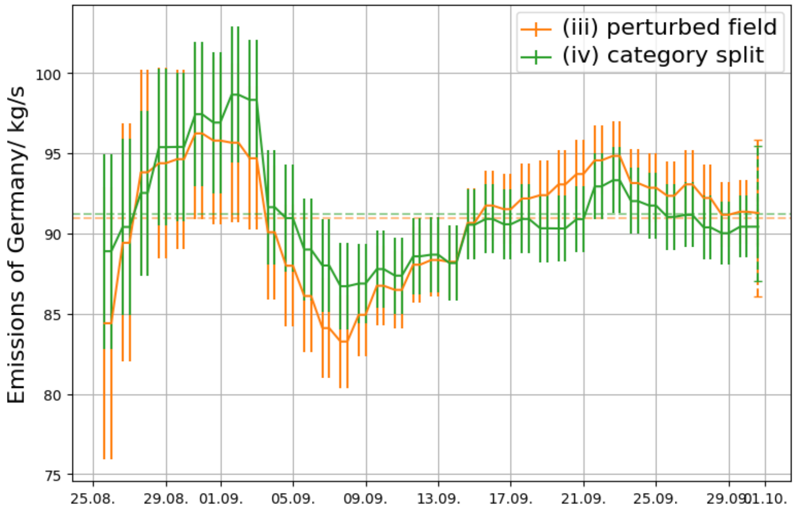

Figure 6. The evolution of the emission posterior and its ensemble uncertainty for Germany throughout the month. The dashed line shows the average starting from the first of the month and the error bars on the right its uncertainty.

small increases in the uncertainty can lead to large changes in the relative standard deviation. Lastly, some point-like source, such as Paris and the Upper Silesian Coal Basin, also have increased uncertainties. We discuss point-like sources in Section 5.6.

With enough observational coverage, such as in Germany and BeNeLux, the uncertainty decreases. Other regions, like western France or the Iberian peninsula would benefit from more observational coverage.

In the boundary regions, such as Ireland, Crete, and Sicily, it might be difficult for the method to differentiate inflowing boundary data bias and emission corrections. As the concentration passes into the observationally covered region, this should be mitigated and any boundary data bias reduced.

4.1.2 Category Split Approach Application

Here, we discuss the simulation (iv) with the category split approach using a sample month, focusing on the difference to (iii) from the previous subsection. A single assimilation step is shown in Figure 8, where we show some of the updates to the category scale factors and the resulting change in the emission field. As before, the change in concentrations is distinct from the change in the emission field. In contrast to Figure 4, the change in the emission field has sharp edges, due to the category split.

In the category split, we can calculate the cross correlation between the scale factors of the different categories. Large negative correlations can imply that the categories are difficult to differentiate. The cross correlation of the scale factors of the German categories for the sample month is shown in Figure 9. There are some negative correlations, the largest one between the agriculture (NW.KL) and non-agriculture-non-natural sectors (NW.nKLN) in Northrine-Westphalia (NW). This implies that these two sectors are difficult to differentiate, their sum can most likely be resolved better. There are also correlations

https://doi.org/10.5194/egusphere-2026-3221
Preprint. Discussion started: 7 August 2026

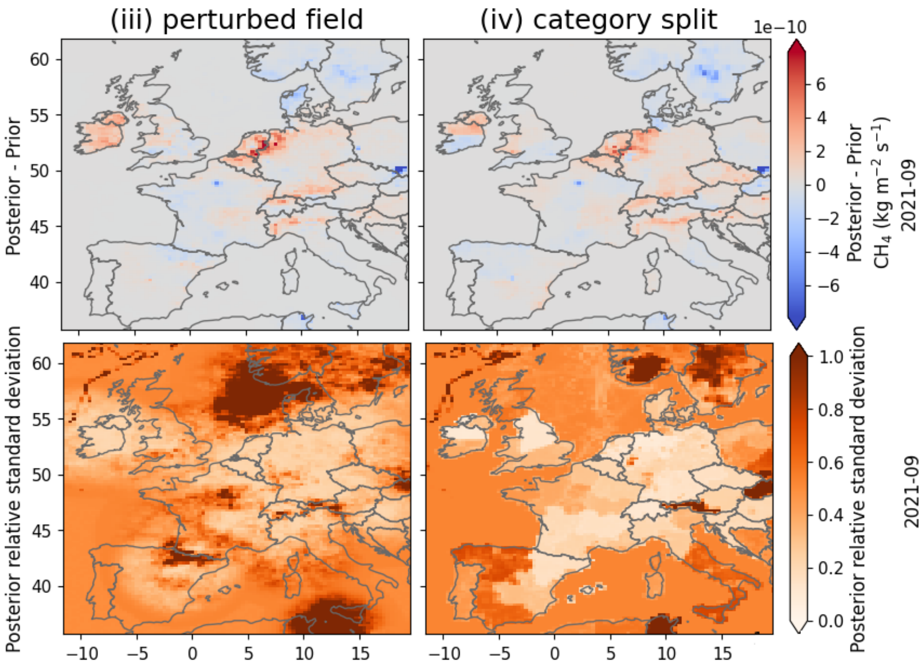

Figure 7. Top: The difference between emission posterior and prior for the two approaches in the sample month. **Bottom**: The relative pointwise standard deviation of the posterior. Plots were created with FLUXIE (Ramsden et al., 2026)

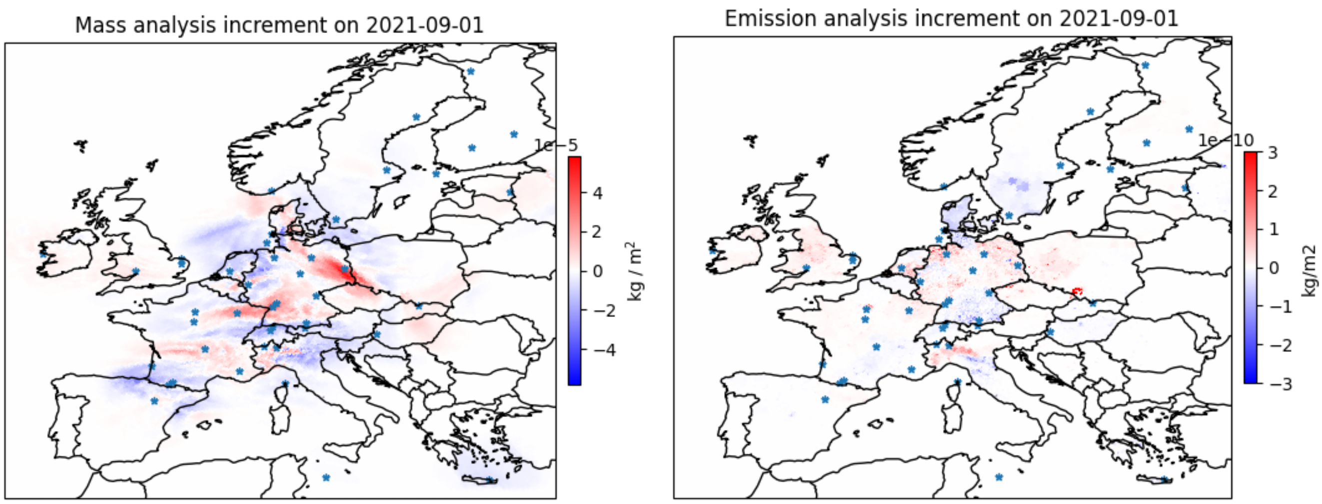

Figure 8. The analysis increment of the (iv) assimilation step for September 1st, 2021. **Left**: The mass increment summed over the height levels after the concentration adjustment. **Right**: The emission increment. The blue dots represent the observation sites used in this assimilation step. The two approaches show similar overall spatial patterns.

https://doi.org/10.5194/egusphere-2026-3221
Preprint. Discussion started: 7 August 2026

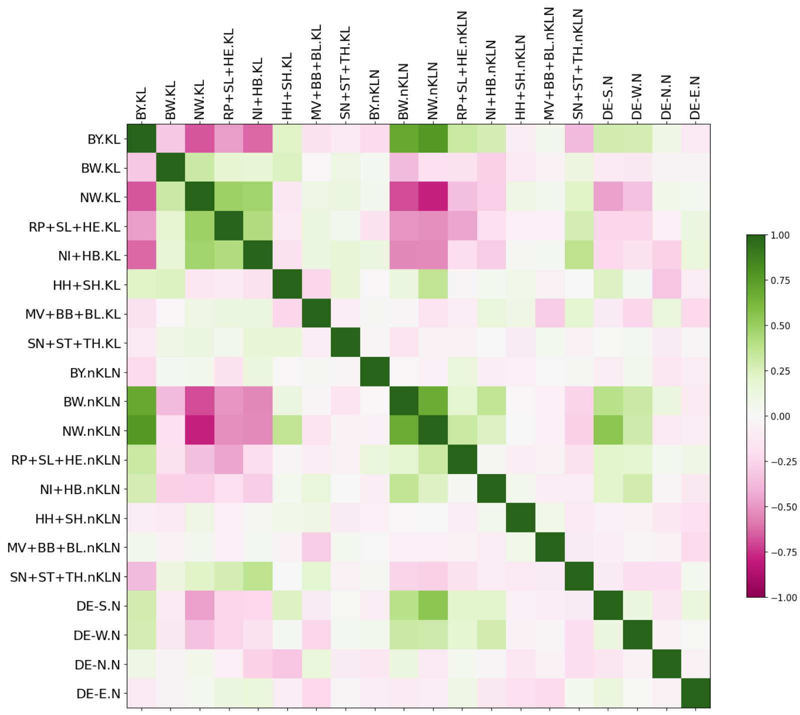

Figure 9. The cross correlation between the scale factors of the German categories for the sample month of September 2021.

between nearby regions as well, like NW and Baden-Würtemberg (BW). Other than that, the correlations are smaller, which implies that the categories can somewhat be differentiated, or the categories are too small to be detected and therefore do not deviate from their prior.

We show a comparison of the resulting posteriors between the two methods in Figure 7. The overall spatial pattern in Central Europe looks similar between the methods, as well as the uncertainty reduction. The (iii) perturbed field approach can have more localized changes, as seen on the German–Dutch border, which (iv) spreads out over a larger area. The largest difference can be seen over the sea, as (iii) does not differentiate between land and sea, while the regional split of (iv) does. On the periphery, where there are less observations, the updates can also differ between the methods, as for example in Ireland or Brittany (Northwestern France). In the latter, this uncertainty is reflected in the relative standard deviation. The uncertainty fields look similar between the methods as well.

4.1.3 Analysis Mass Increment

As we have seen in the previous section, the emission and concentration adjustments do not necessarily align spatially. This opens up the question of how these corrections behave in relation to another. It could be that the method uses the newfound freedom in the state space to correct emissions in one direction and adjust concentrations in the other perpetually, creating

https://doi.org/10.5194/egusphere-2026-3221
Preprint. Discussion started: 7 August 2026

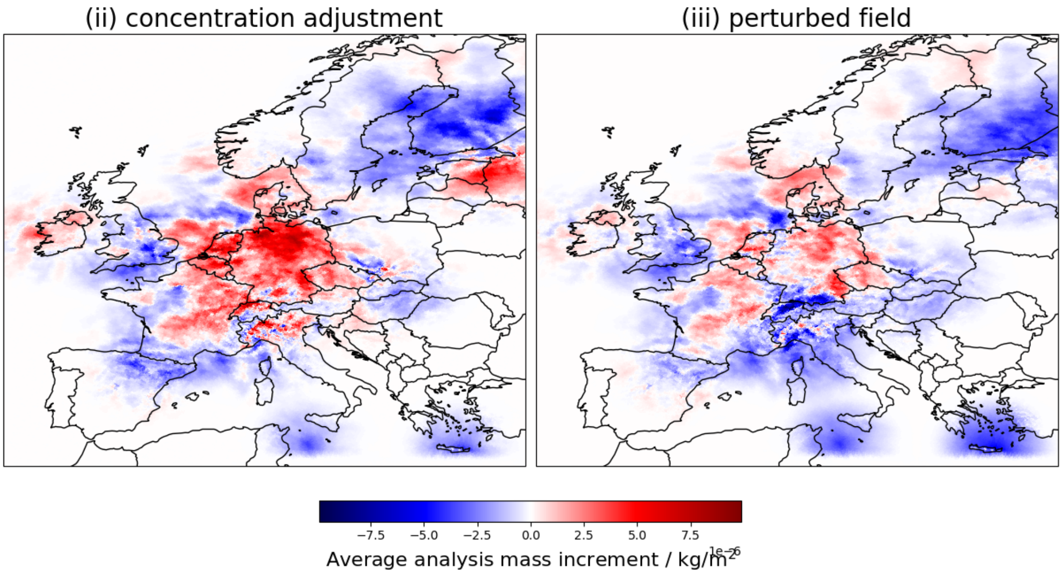

Figure 10. The temporally averaged analysis mass increment over the sample month for the (ii) concentration adjustment and the (iii) perturbed field approach. The concurrent assimilation needs to correct less overall mass.

an erroneous image. In this section, we show that this is not the case, and that the emission corrections alleviate the need for correcting concentrations.

For the simulations (ii)-(iv), we can calculate the analysis mass increment (AMI) for each assimilation step. This is calculated by comparing the forecast concentration field and analysis concentration field after each daily assimilation step and summing over the vertical level to obtain the horizontal distribution. For the (ii) concentration adjustment, and the (iii) perturbed field method, the spatial distribution is shown in Figure 10. It can clearly be seen that the concurrent adjustment of emissions reduces the absolute value of the AMI in Central Europe. This can be interpreted as reducing the need for correcting concentrations in the assimilation step, because they have been created by correcting the emissions previously.

To further this inquiry, we can look at the temporal evolution of the AMI over Germany, and compare it to the change in emissions. This is shown in Figure 11. First, we show the AMI for (ii) and (iii) over Germany for each daily assimilation step. There is considerable scatter in the AMI, which depends on the boundary data, the emissions, and the previous assimilation step. Still, the concurrent adjustment (iii) needs to correct less mass systematically throughout the month. We label this difference as $\Delta\mathrm{AMI} = \mathrm{AMI}_{(iii)} - \mathrm{AMI}_{(ii)}$, and we can estimate the amount of emissions this corresponds to by dividing through the assimilation time period $\Delta t = 1\,$day. This is shown alongside the change in emissions in the second panel of Figure 11. Here, while there is scatter in the ΔAMI, a moving average would be roughly below the emissions adjustment. This is to be expected, since the (ii) concentration only adjustment has less spread in the concentration ensemble and effectively less freedom.

This indicates that some of what (ii) has to correct in concentrations, (iii) can correct in emissions. This also indicates that the decrease in AMI is primarily due to local corrections to emissions, and not sourced outside of Germany.

https://doi.org/10.5194/egusphere-2026-3221
Preprint. Discussion started: 7 August 2026

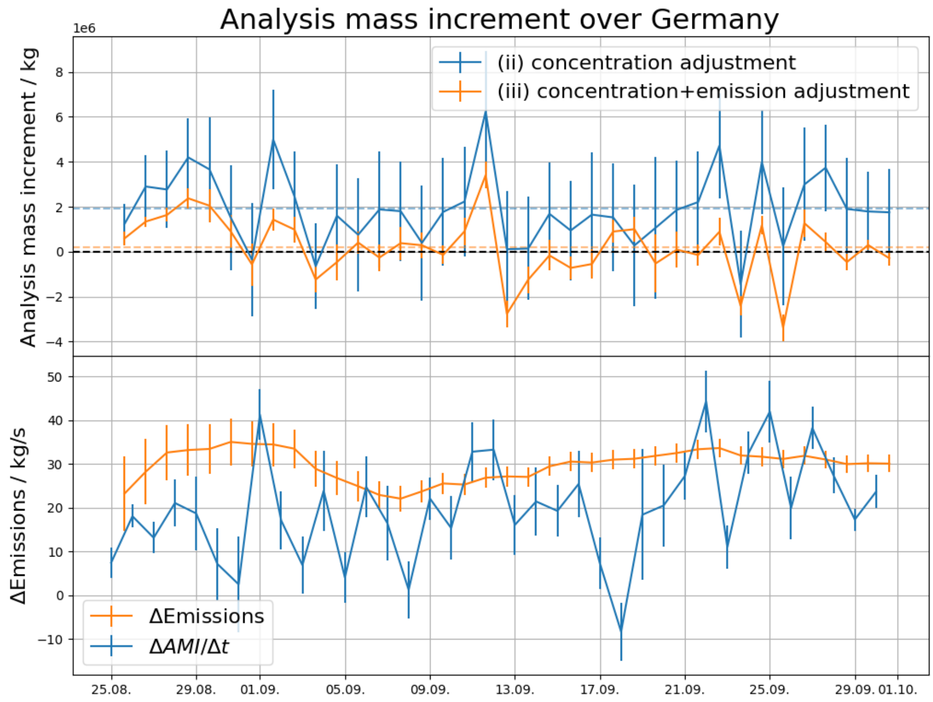

Figure 11. Top: The analysis mass increment in Germany throughout the month for the two different adjustments (ii) and (iii). The error bars represent the ensemble spread, and the dashed lines the monthly averages. The concurrent adjustment (iii) consistently adjust less CH_4 mass than the concentration only adjustment (ii). **Bottom**: The change in German emissions (see Figure 6), compared to the difference in the average analysis mass increment between (ii) and (iii) $\Delta\mathrm{AMI}/\Delta t$.

The approach (iii) reduces the average AMI very closely to 0. While the mass is not conserved explicitly in the method, an average AMI of 0 corresponds to mass conservation on average (over Germany). Whether this is a desirable goal of the method is questionable though. It would require the boundary data coming into Germany to be unbiased. This could be an indicator that any incoming boundary data bias is successfully reduced from the observation sites on the boundary. Alas, tracer mass is not strictly conserved in ICON–ART itself, as we discuss in Section 5.6, such that this is a difficult benchmark to evaluate.

Overall, the evolution of the AMI compared to the emissions is a sanity check for the method. It seems that the newfound freedom in the state space is used effectively to reduce the mass correction, and not, e.g., in the opposite direction.

4.2 Parameter selection

In this section, we explore the hyperparameters of the methods that we have described initially, and how their choice affects the result for the sample month of September 2021. First for the approach (iii) with the perturbed field method, and then for the (iv) category split.

https://doi.org/10.5194/egusphere-2026-3221
Preprint. Discussion started: 7 August 2026

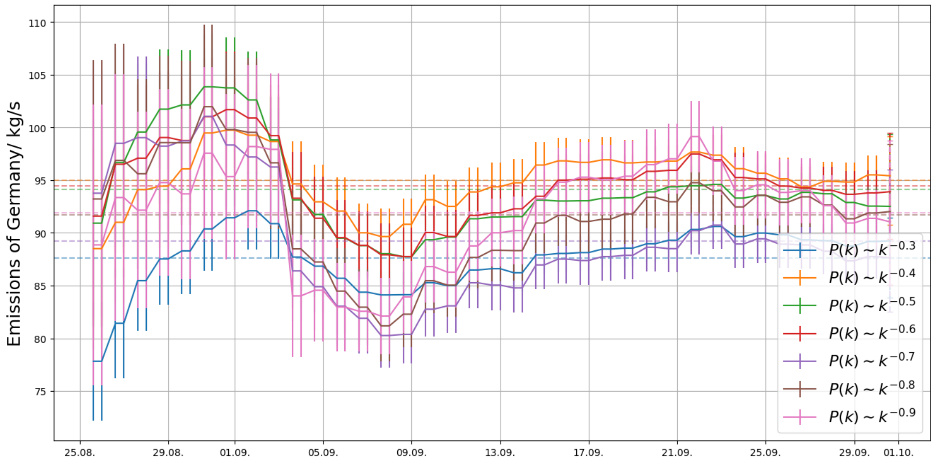

Figure 12. The estimates of the German emissions throughout September 2021 for different power law indices. The overall patterns are similar in between the different correlation structures.

4.2.1 Perturbed Field Approach Parameters

Power Law Index of the Gaussian Random Field

The most prominent choice in the perturbed field approach is that of the power law index α of the scale-free gaussian random field. While the underlying mathematical field is scale-free, with a finite grid resolution, we introduce a scale into this field. This affects the length scale of the corrections that are introduced into the emission field. In Table 3, we show the effective correlation length of the power law indices, where the correlation between points drops to $\sim 50\%$. A smaller α gives a smaller effective correlation scale and smaller emission increments. A larger α with larger effective correlation scale also means a larger prior uncertainty – given a fixed point-wise uncertainty – on national scales, e.g. Germany.

The estimates of the German emissions for different α throughout the sample month are shown in Figure 12. Initially, a larger power law index translates to larger corrections. The aforementioned effect of the larger uncertainties can also be seen in the error bars. Over time, the curves have qualitatively similar behavior and converge to a value around $\sim 90\,\text{kg/s}$. While there is some spread, the results are within the uncertainty of each other.

In Figure 13 we show the emission posteriors for four different power law indices. The relative posterior increase has very similar spatial patterns in between the methods, but a larger power law index gives a more smooth distribution, due to the larger correlation scales. The most prominent differences can be seen on the Iberian peninsular, where there is little observational coverage. The relative standard deviation of the posterior also reflects the uncertainty assumptions. A larger power law results in a larger-scale and more smooth reduction of the uncertainty. For the smaller power laws, there are more points which appear uncertain. This contrast is most prominent in France. In Germany and BeNeLux on the other hand, the reduction of the uncertainty seems mostly independent of the power law index.

To have a conservative estimate of the correlations, we ultimately choose a power law index of $\alpha = 0.5$.

https://doi.org/10.5194/egusphere-2026-3221
Preprint. Discussion started: 7 August 2026

Power Law Index α	Effective Correlation Length
0.3	10km
0.4	40km
0.5	100km
0.6	200km
0.7	500km

Table 3. The effective correlation length, where the correlation drops to $\sim 50\%$, for different power law indices.

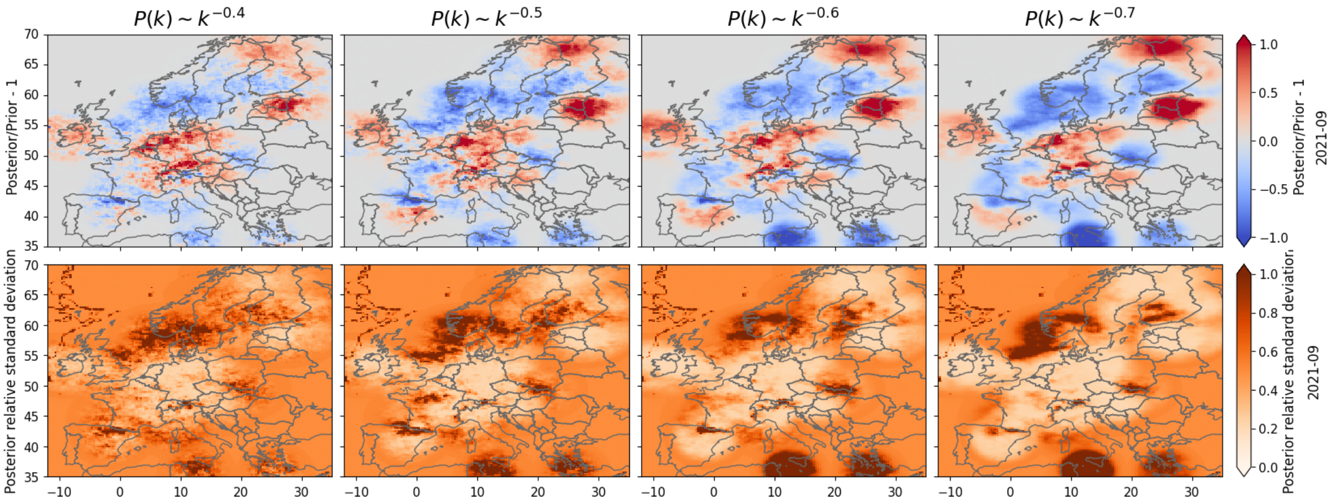

Figure 13. Top: The relative increase of the posterior over the prior for the different power law indices. **Bottom**: The relative point-wise standard deviation of the posterior. Larger power law indices translate to a smoother field.

This method can be further refined in the future, where the correlation scales are based on the emission sectors. For example, it is a reasonable expectation that natural fluxes have larger scale correlations than emissions based on heating in urban areas. In future research, we could explore different choices of power law index for different regions and anthropogenic sectors, and what this tells us about the uncertainty structure of the underlying emission fields.

Uncertainty Inflation

The uncertainty inflation factor ρ_p for the emission state vector is something specific to the method, for which there is no inherent best value or physical intuition. Since the emissions are stationary and do not move out of the domain like the concentrations do eventually, the value has to be carefully chosen as to not increment the ensemble uncertainty indefinitely.

The relative posterior uncertainty for $\rho_p = 1.005, 1.01, 1.02$ is shown in Figure 14. Recall that the posterior uncertainty is a combination of the ensemble spread and the temporal standard deviation. The inflation factor primarily influences the former, but has an indirect effect on the latter. In the figure, you can see the effect of the localization of the LETKF. For larger ρ_p, the uncertainty on the edges of the localization radius increments as there is not enough information available, as can be

https://doi.org/10.5194/egusphere-2026-3221
Preprint. Discussion started: 7 August 2026

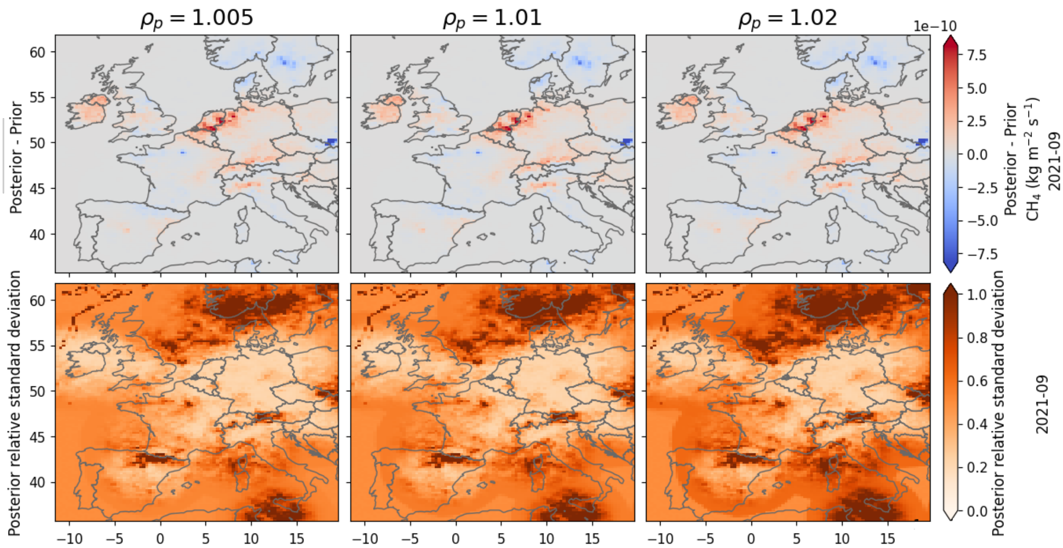

Figure 14. Top row: Difference between posterior and prior for three different uncertainty inflation parameters $\rho_p = 1.005, 1.01, 1.02$. **Bottom row**: The point-wise relative standard deviation of the posterior.

easily seen, e.g. on the Iberian peninsula. Other locations that are large point sources, such as Paris or the Upper Silesian Coal Basin, can also have larger uncertainties, probably due to temporal variations that the model sees. While the sources might be constant themselves, transport uncertainties and the double penalty issue may make it seem to the method that there are temporal variations (for a discussion, see B25).

Overall, the posterior innovation between the three inflation factors has an almost identical spatial structure. The larger difference is in the uncertainty estimate of the posterior. While the spatial structure is still similar, the localization effects are more strongly visible for the larger inflation factor. Still, Central Europe has a consistent reduction of the uncertainty regardless of the inflation factor. Ultimately, we choose the smallest inflation factor presented here, to reduce the localization effects.

Other Parameters

For the other parameters that are used in approach (iii), we show a short overview of their effect on the total German emissions in Figure 15. Most of the parameter choices have a small effect on the posterior, but they are all within each other's uncertainty.

4.2.2 Category Split Parameters

In contrast to the (iii) perturbed field approach, the (iv) category split does not have a parameter for the correlation length, but the choice lies in the regional categorization. Due to computational costs, we do not try to explore the space of regional categories here, but leave this to future research.

https://doi.org/10.5194/egusphere-2026-3221
Preprint. Discussion started: 7 August 2026

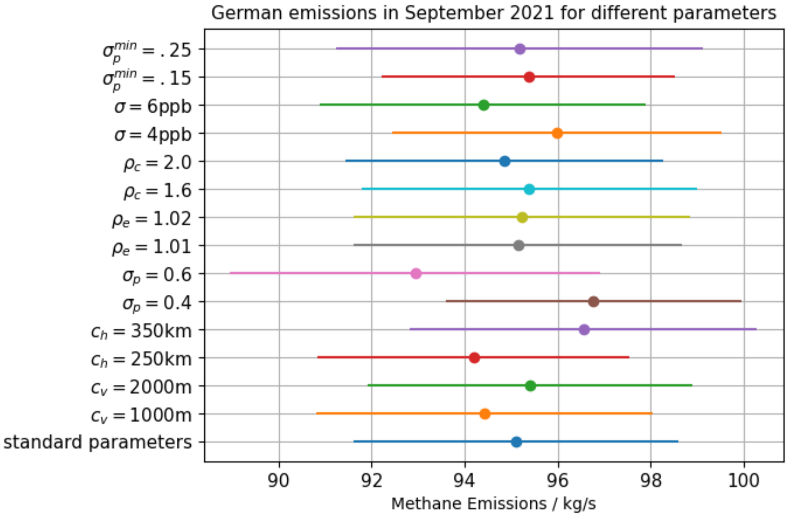

Figure 15. The posterior and the 1σ uncertainty of the total German emissions for the sample month for different choices of parameters in the (iii) perturbed field approach.

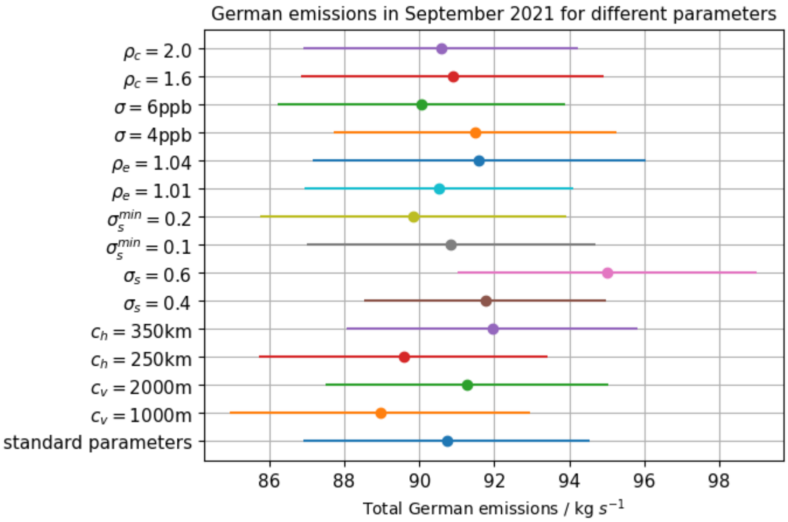

Figure 16. The posterior and the 1σ uncertainty of the total German emissions for the sample month for different choices of parameters in the (iv) category split approach.

The other parameters behave similarly to the (iii) perturbed field approach. We do not explore them in detail here, but only show an overview of them in Figure 16. As before, most of the parameter choices have a small effect on the posterior, but they are all within each other's uncertainty.

https://doi.org/10.5194/egusphere-2026-3221
Preprint. Discussion started: 7 August 2026

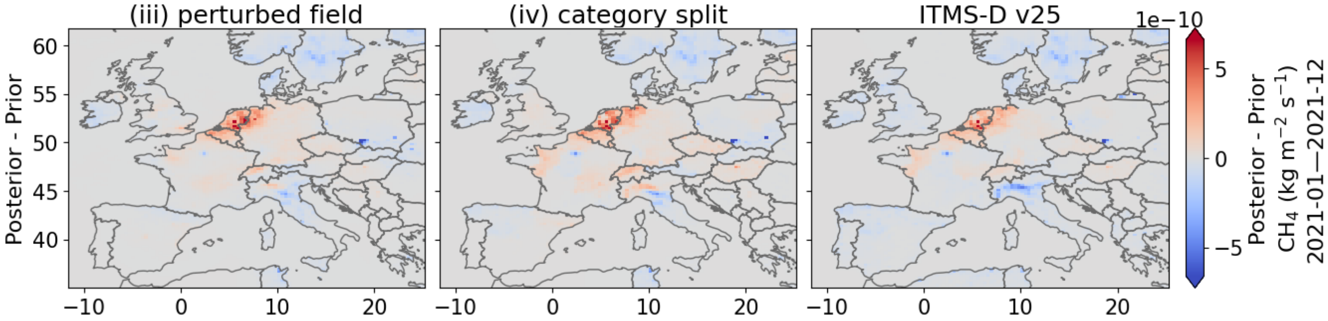

Figure 17. The innovation in the emission posterior for 2021. Shown are three approaches, **Left**: (iii) the perturbed field approach, **Middle**: (iv) the category split, and **Right**: the ITMS-D v25 results. The plot was produced with FLUXIE (Ramsden et al., 2026)

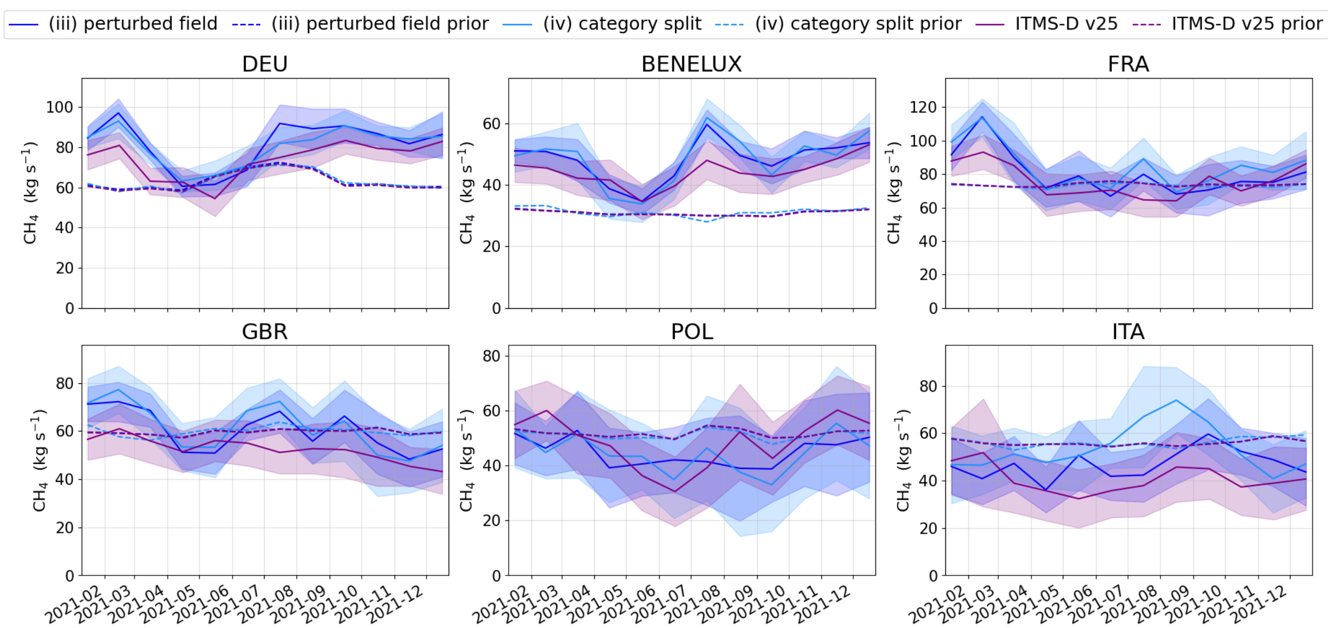

Figure 18. The timeseries of the results for 2021 for different regions in Europe. Shown are the 2σ confidence intervals.

5 Results & Discussion

375 In this section, we present the resulting methane emission estimates of 2021. We compare the features of our two approaches here also to the synthesis inversion presented in *B25*, with the results published in Bruch et al. (2026). We refer to these results as ITMS-D v25.

https://doi.org/10.5194/egusphere-2026-3221
Preprint. Discussion started: 7 August 2026

5.1 Methane Emissions of 2021

The aggregated results for the monthly inversions are shown in Figure 17 and Figure 18. Figure 17 shows the innovation of the emission field, i.e. the difference between posterior and prior. It can be seen that the two approaches which adjust concentrations and emissions concurrently with either, (iii) perturbed emissions or the (iv) category split produce on average very similar results with a similar spatial pattern. The regional category borders can be seen for (iv), while the results of (iii) are more smoothly distributed spatially. In Germany and BeNeLux the spatial patterns match very well between the methods. There are visible differences in the Northwest of France. Here, it might be beneficial to split the regions of Normandy and Pays de la Loire apart in the category split. In Italy, the methods show the clearest differences. In the Po valley, there are difficulties modeling the region and the observation sites.

The comparison with ITMS-D v25 also shows very similar spatial patterns. The largest difference is also seen in Italy. Here, the results could partially be explained by the exclusion of the site in Ispra (ISP) in *B25*. Another difference is visible in the British Isles, ITMS-D v25 corrects the whole region downward, while there are local differences in (iii) and (iv). This might be due to different treatment of the boundary data.

The time series data shown in Figure 18 also shows general agreement between the three methods, especially in Central Europe. The trend in Germany and BeNeLux is similar, while the results here are slightly above those of *B25*. There are large differences and uncertainties in Italy, due to the aforementioned special treatment, different observation site selection and modeling difficulties. Interestingly, the (iv) category split produces results closer to the prior in Italy, and (iii) is closer to ITMS-D v25 even though these methods differ significantly. Looking at the curves in Figure 18, the ITMS-D v25 results seem smoother overall compared to the methods (iii) and (iv).

For the (iv) category split, we can compare the resulting scale factors directly to ITMS-D v25. This is shown in Figure 19. If the methods produce the same scale factor, it will lie on the diagonal. Most categories appear close to the diagonal, with some visible outlier such as the Northwest of Italy. The German and Dutch categories are highlighted and are all along the diagonal. For for the (iv) category split, agricultural sectors (.NL) lie above the diagonal, while the rest (.nKLN) is generally below. This could be explained by the fact that ITMS-D v25 assumes a regional correlation between the .KL and .nKLN sectors, therefore forcing them to be corrected together and balancing them out somewhat, while the approach (iv) here does not make this assumption.

The time series for the sectorial decomposition in Germany is shown in Figure 20. Again, the curves overlap within in the uncertainties and most of the change in German emissions is attributed to the agricultural sector. Also the post-hoc sector attribution of (iii) gives comparable results, albeit a little lower for agriculture.

Our results show significantly higher CH_4 emissions in 2021 in Germany compared to the reported emissions (UNFCCC submission 2025), the perturbed field approach (iii) gives an increase of $33 \pm 20\,\%$, and the category split (iv) shows $32 \pm 16\,\%$. This is primarily attributed to the agricultural sector by (iv), showing a $44 \pm 26\,\%$ increase compared to the prior. In the Netherlands, we find an increase of the total emissions of $51 \pm 22\,\%$ and $49 \pm 24\,\%$ for the methods, respectively.

https://doi.org/10.5194/egusphere-2026-3221
Preprint. Discussion started: 7 August 2026

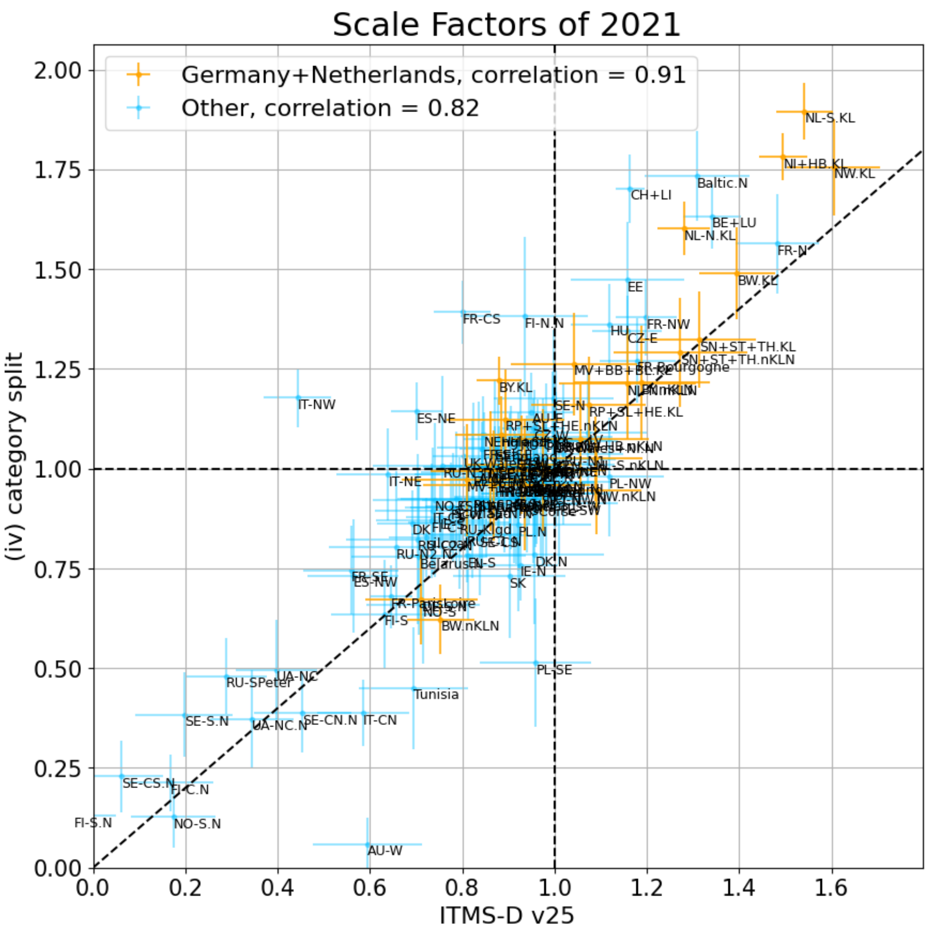

Figure 19. The results for the scale factors of the (iv) category split and ITMS-D v25. Categories that have the same resulting scale factor lie on the diagonal. Highlighted are the German and Dutch categories, which have an overall correlation of $\sim 91\,\%$. The others have a correlation of $\sim 82\,\%$.

https://doi.org/10.5194/egusphere-2026-3221
Preprint. Discussion started: 7 August 2026

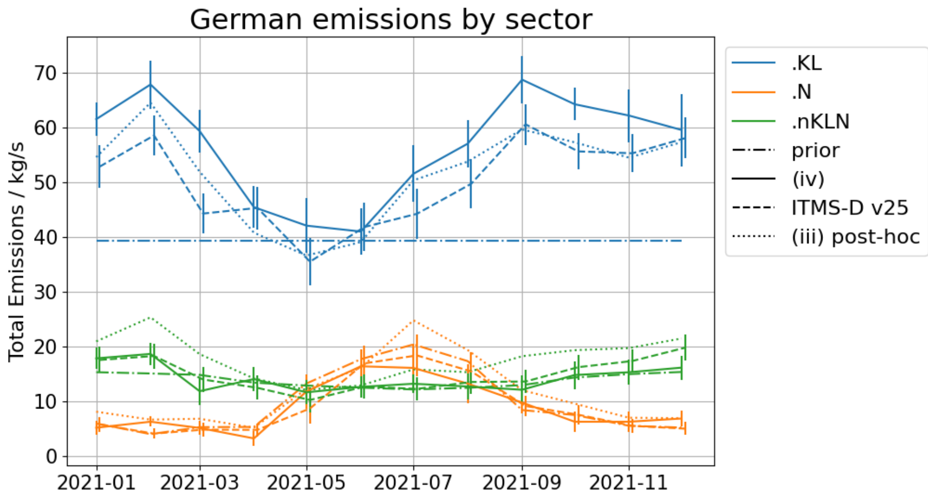

Figure 20. The sector decomposition results in Germany, given by method (iv), ITMS-D v25, and the post-hoc sector attribution of (iii). The differentiated sectors are agricultural (.KL), natural (.N), and the remains(.nKLN). The three methods give similar results.

The RMSE and its skillscore is shown in Figure 21. It can be seen that the concurrent assimilation generally improves the RMSE, except for February[4]. Also, there seems to be a seasonal pattern, where the methods perform best in the summer. This might be due to several factors, e.g. seasonal differences in atmospheric mixing of the GHG, or different emission patterns. Also, we have explored the hyperparameter space in the month of September, maybe these are seasonally dependent. We need to model more years to see if this pattern holds up. We leave the exploration of this to future research.

5.2 Comparison of the two approaches

We have presented two approaches for the assimilation of emissions, which work in complementary ways.

The category split (in Germany) needs a detailed spatial decomposition of each economic sector, which is more than is required by countries within UNFCCC reporting guidelines. This information has to be obtained elsewhere for the validation, such as the national reporting agencies or the CAMS-REG-ANT dataset. The results of the category split – if accurate – are more useful for policymakers, who have to think of and assess policy within the anthropogenic emission sectors. But as discussed previously, this can be difficult and there is a risk of misattribution. This is especially the case for uncataloged or unexpected sources, e.g. gas leaks.

The perturbed field approach needs less information for its application, it only assumes a correlation based on distance. On the one hand, it disregards the large scale correlations induced by human activity and government policy, and needs large observational cover to correct for this. On the other hand, it has a larger state space and is not bound by country or regional borders, which can be an advantage, depending on the circumstances. The perturbed field approach can help find where the

[4]It seems that in February, a single station in Switzerland is responsible for dragging down the RMSE. The Cumulative Ranked Probability Score (CRPS), which takes into account the ensemble uncertainties, still improves for the concurrent assimilation.

https://doi.org/10.5194/egusphere-2026-3221
Preprint. Discussion started: 7 August 2026

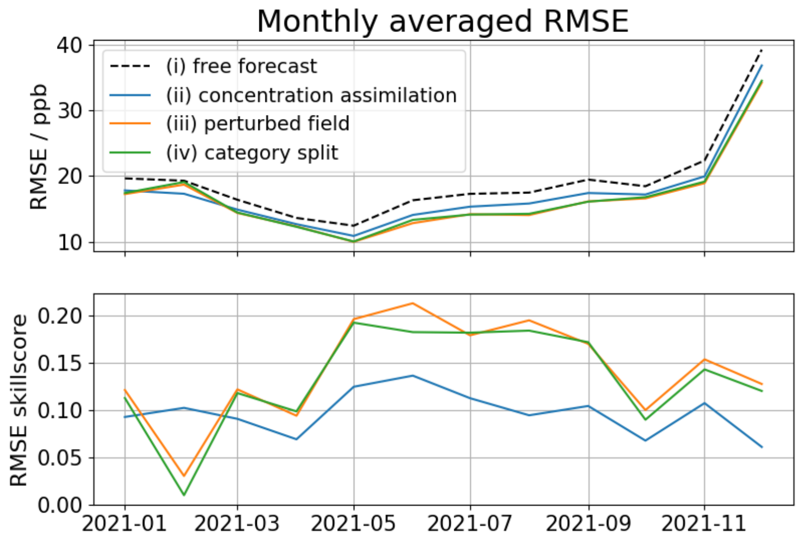

Figure 21. The RMSE and its skillscore for each monthly simulation. The concurrent assimilation generally results in a larger reduction of the RMSE.

category split is insufficient and should be broken into smaller regions for example. The approach can also more easily be used for near-real-time emission estimation, as the national emission reporting and sectorial decompositions lag behind by at least one year, usually.

It is remarkable that the two methods give such similar result, despite the vastly different prior error structures, see for example the work by Munassar et al. (2023).

5.3 Comparison to other methods

As we have already discussed, the comparison to the ITMS-D v25 results of the method of *B25* shows overall agreement, especially in Germany and the BeNeLux region.

On a methodological level, the concurrent assimilation of fluxes and concentrations with both approaches differ significantly from the synthesis inversion of *B25*. The latter computes a far-field correction based on large-scale differences between boundary data and observations, while the methods here rely on a localized correction of the CH_4 concentration to correct the boundary data, as it moves through the domain. It is reassuring to see the results being so closely aligned, despite these differences.

The curves presented in Figure 18 seem more ‘rough‘ for the methods presented here, compared to *B25*. This could be due to several factors. First, the methods here are initialized every month individually, while *B25* uses a single initialization for its simulation. Second, as the assimilation presented here reduces the uncertainty in the emission estimate, the observations at the beginning of the month have more weight compared to the later ones. This could also lead to a less smooth result.

https://doi.org/10.5194/egusphere-2026-3221
Preprint. Discussion started: 7 August 2026

On a technical level, the methods also differ significantly, and each have their own advantages. First, the methods presented here are *online*, adjusting the emissions while running. In comparison, *B25* is *offline*, adjusting the emissions after the simulation, for which it is computationally much cheaper to run many inversions with different hyperparameters. For the category discrimination, the method presented here generally needs a larger ensemble size, but it does not need an individual tracer for each category, so the methods have different trade-offs in computational cost.

The results presented here are also qualitatively in line with other publications. The discrepancies in emission reporting of Germany and the Netherlands are also found for previous years by Bergamaschi et al. (2022); Petrescu et al. (2023); Steiner et al. (2024a); Ioannidis et al. (2026), and for 2021 by Ganesan et al. (2026); Manning et al. (2025), but are well below the 67 % increase in Germany seen by East et al. (2025) for the year 2023.

The general agreement between the posterior emissions and reporting seen in Great Britain and Ireland is in line with Bergamaschi et al. (2022).

5.4 Differentiating sectors

In Germany and the Netherlands, we try to distinguish agriculture and natural+lulucf from the rest of the emissions. In the (iv) category split, we use the spatial sector information in the prior to create a category and scale this with a factor that is assimilated. This is similar to the synthesis inversion method in *B25*. In contrast to our previous publication, here, we have assumed no correlation between different sectors within Germany, but drawn uncorrelated initial distributions, yet we still arrive at very comparable results, as seen in Figure 20 and Figure 19. Still, as seen in Section 4.1.2, there are some correlations in the posterior of the scale factors in Germany, which implies that the sector attribution should be handled with caution. Both methods potentially suffer from the same bias: If the observations are not sufficient to distinguish sectors based on their spatial distribution, the method can still adjust the total emissions. In such cases, changes in the total emissions will likely be attributed to the sector with the largest absolute uncertainty, which is the largest sector, agriculture (see discussion in *B25*).

As a cross-check, we can compare with the post-hoc sector attribution of (iii). This method should not have the aforementioned bias. Here, it assumes that the gridpoint-wise distribution of the sectors is correct. The attribution to agriculture is systematically below (iv), and that to the rest is above, but the differences seem small. This difference is most likely explainable due to the aforementioned attribution effect. Most of the seasonal cycle is still attributed to agriculture nonetheless.

Since these three different approaches give similar results, this strengthens the trust in the sector attribution capabilities of the methods. Note that if there is not sufficient information in the transport modeling to differentiate sectors, even similar results might be insignificant.

5.5 Seasonal Cycle

In *B25*, the authors have already discussed the somewhat unexpected seasonal cycle in Germany, where there is a minimum in the emissions in spring, while rising towards the latter part of the year. This is unexpected for the agriculturally dominated emission, this sector would be expected to have a roughly constant flux throughout the year. We have reproduced this seasonal cycle – within the uncertainties – here with alternative inversion methods. While we use the same boundary data, the CH_4

https://doi.org/10.5194/egusphere-2026-3221
Preprint. Discussion started: 7 August 2026

concentrations in Germany are not subject to a far field correction as in *B25*. In *B25* it was argued that a seasonal bias in the boundary data could be a cause for the seasonal differences in the emissions. Since we treat the boundary data very differently here, yet arrive at the same pattern, this seems more unlikely. The other possibilities, such as the neglect of the OH sink of CH_4 (Logan et al., 1981) or seasonal meteorological differences cannot be ruled out and are discussed further in the following section.

5.6 Limitations

One of the biggest limitations is the localization of the LETKF. We can only correct the emissions and concentrations around the observation sites, which are unevenly distributed in Europe. The observational coverage is dense enough only in Central Europe to result in accurate estimates.

In the setup that we have shown, the observations at the beginning of a month have more impact on the emissions than the later ones, as the emission uncertainties are reduced. If the assumption of constant fluxes does not hold, as reality is usually more complicated, this will bias the emission posterior to the beginning of the month. However, it is difficult to tune the uncertainties of the emission ensemble such that all regions do not diverge or converge too early.

Also, there are limitations inherent to ensemble based methods, such as the LETKF. While they may produce a good estimate of the mean, they can fail to predict the covariance correctly, especially for correlation lengths approaching grid size (Gilpin, 2025; Gilpin et al., 2025). Furthermore, it is difficult to model point sources, as seen in the Upper Silesian Coal Basin, discussed more in depth in *B25*. Here, a plume emitted by the point source might reach the observation site or not, depending on the ensemble member. In this case, the Gaussian uncertainty approximation by the ensemble breaks down. This is difficult to treat with the LETKF, which assumes Gaussian uncertainties throughout.

Another limitation is the transport model. One particular issue is with wet air mass changes, due to the technical setup and physical assumption implemented in ICON–ART. ICON itself conserves the total air mass. When wet air mass changes – e.g. due to precipitation or evaporation – ICON assumes this is compensated by a respective (unphysical) change in dry air mass (Prill et al., 2024). ICON-ART models the tracer transport in the mass mixing ratio with regard to wet air mass, while the observations of GHGs are generally with regard to dry air mass. The initial data from CAMS is also available w.r.t. dry air mass, so we have to convert between the two back and forth. After transport, when the wet air mass changes, the dry air mass is artificially compensated, resulting in an inaccurate conversion. For example, when evaporation happens during transport, the wet air mass is increased. As a result, the dry air mass is decreased artificially. The conversion then divides by this dry air mass fraction, and the estimated CH_4 concentration is artificially larger (Malardel et al., 2019). It has yet to be determined how, and to what degree, this affects emissions and the observed seasonal cycle. This issue of inaccurate conversion is subject of ongoing and future work.

https://doi.org/10.5194/egusphere-2026-3221
Preprint. Discussion started: 7 August 2026

5.7 Implications for future research

There are several avenues open for future research. The first one is the inclusion of more observations, especially satellite observations. This would help get around the localization problems of the LETKF and allow for emission estimates throughout the model domain.

Another avenue is an exploration of different generation processes for the perturbed field method (iii). In this paper, we have assumed a Gaussian random field, but there is no inherent ‘best‘ method for this problem. We could assume different perturbation mechanisms for different emission sectors or different scales for different regions. We could also combine (iii) and (iv) by spatially perturbing the individual categories, and using more physically motivated assumptions for the uncertainty structure.

Speaking of the uncertainty structure, we could also look at different uncertainty inflation approaches, to prevent divergence or early convergence of the ensemble uncertainties, such as those explored in Bisht et al. (2023).

The perturbed field method (iii) can be extended to also allow for temporal perturbations. This can be utilized to treat non-constant emissions, such as in the case of the diurnal cycle of CO_2. We will investigate the application of this method for the validation of CO_2 and N_2O emissions.

6 Conclusions

We presented an assimilation system for CH_4 concentrations and emissions for the purpose of validating national emission reporting, based on ICON–ART and close to the operational NWP at the DWD.

We have adjusted the concentrations and emissions concurrently by augmenting the state vector of a 4D-LETKF system. We have explored the relation between concentration and emission analysis increments and found that adjusting emissions relieves the need for correcting concentrations. We have introduced two approaches to adjust emissions, one based on a perturbed field approach, and one on a split into regions and economic sectors. We have shown that both approaches agree with each other in Central Europe and that the results are stable when varying the hyperparameters.

We applied this system in Central Europe for the year of 2021 and found significantly higher emissions in Germany and the BeNeLux region compared to the national reporting. The two approaches show an increase of $33 \pm 20\,\%$, and $32 \pm 16\,\%$ of the German emissions in 2021. The methods primarily attribute this to the agricultural sector. We have shown that these results are consistent with our previous publication, utilizing a synthesis inversion method (Bruch et al., 2025b). These findings provide additional confidence in the inversion methods, which should be further assessed using different transport models and observations.

This publication is part of a novel, modular system we are developing at the DWD with the long-term goal of validating national emission reporting. Future developments will include the integration of satellite data and extension to additional GHGs, paving the way for comprehensive validation of emissions in Germany and Europe.

Author contributions. NB conceptualized the data assimilation setup, with support from NK, VB, TR, and RP. NB implemented the approaches based on code from NK, and performed the investigation. NB wrote the original draft together with AKW. TR and MS configured the transport model and orchestrated the cycling. TR, VB, and BE interpolated the a priori flux data which BE collected. DJCO and MS organized data streams of CH4 concentrations and observations. DJCO, MS, TR and VB contributed to testing and tuning the transport model. AKW supervised and coordinated the project. All authors reviewed and edited the manuscript.

Competing interests. The authors declare that they have no conflict of interest.

Acknowledgements. We thank Stefan Feigenspan, Christian Mielke, Theo Wernicke, Hannes Imhof, John Akubia, Roland Fuß and Hannes Witt for helpful discussions and providing a priori emission fields. We thank Frank-Thomas Koch, Christoph Gerbig, Dominik Brunner, Michael Steiner, David Ho, Thomas Kaminski, and our partners in the ITMS project for very helpful and inspiring discussions. We thank Milad Ghanbarpour for an early draft of the base LETKF implementation. We also wish to thank Peter Bergamaschi, Aurélie Colomb, Martine De Mazière, Lukas Emmenegger, Dagmar Kubistin, Irene Lehner, Kari Lehtinen, Markus Leuenberger, Cathrine Lund Myhre, Michal V. Marek, Simon O'Doherty, Stephen M. Platt, Christian Plaß-Dülmer, Francesco Apadula, Sabrina Arnold, Pierre-Eric Blanc, Dominik Brunner, Huilin Chen, Lukasz Chmura, Łukasz Chmura, Sébastien Conil, Cédric Couret, Paolo Cristofanelli, Grant Forster, Arnoud Frumau, Christoph Gerbig, François Gheusi, Samuel Hammer, Laszlo Haszpra, Juha Hatakka, Michal Heliasz, Stephan Henne, Arjan Hensen, Antje Hoheisel, Tobias Kneuer, Eric Larmanou, Tuomas Laurila, Ari Leskinen, Ingeborg Levin, Matthias Lindauer, Morgan Lopez, Ivan Mammarella, Giovanni Manca, Andrew Manning, Damien Martin, Frank Meinhardt, Meelis Mölder, Jennifer Müller-Williams, Steffen Manfred Noe, Jarosław Nęcki, Mikaell Ottosson-Löfvenius, Carole Philippon, Joseph Pitt, Michel Ramonet, Pedro Rivas-Soriano, Bert Scheeren, Marcus Schumacher, Mahesh Kumar Sha, Gerard Spain, Martin Steinbacher, Lise Lotte Sørensen, Alex Vermeulen, Gabriela Vítková, Irène Xueref-Remy, Alcide di Sarra, Franz Conen, Victor Kazan, Yves-Alain Roulet, Tobias Biermann, Marc Delmotte, Daniela Heltai, Ove Hermansen, Katerina Komínková, Olivier Laurent, Janne Levula, Chris Lunder, Per Marklund, Josep-Anton Morguí, Jean-Marc Pichon, Martina Schmidt, Damiano Sferlazzo, Paul Smith, Kieran Stanley, Pamela Trisolino and Giulia Zazzeri for providing the atmospheric observations. NB, NHK, VB, and DJCO acknowledge funding by the German Federal Ministry of Research, Technology and Space (BMFTR) in the ITMS project (grant 01LK2102B) as well as BE (grant 01LK2104A). Maps were plotted with Natural Earth.

https://doi.org/10.5194/egusphere-2026-3221
Preprint. Discussion started: 7 August 2026

References

Arias, P. A., Bellouin, N., Coppola, E., Jones, R. G., and Krinner, G.: Climate Change 2021: The Physical Science Basis. Contribution of Working Group I to the Sixth Assessment Report of the Intergovernmental Panel on Climate Change, Cambridge University Press, Cambridge, United Kingdom and New York, NY, USA, https://doi.org/10.1017/9781009157896.002, 2021.

Basu, S., Lehman, S., Miller, J., Andrews, A., Sweeney, C., Gurney, K., Xu, X., Southon, J., and Tans, . P.: Estimating US Fossil Fuel CO2 Emissions from Measurements of 14C in Atmospheric CO2, Proc. Natl. Acad. Sci. U.S.A., 117, 13 300–13 307, https://doi.org/10.1073/pnas.1919032117, 2020.

Bergamaschi, P., Houweling, S., Segers, A., Krol, M., Frankenberg, C., Scheepmaker, R. A., Dlugokencky, E., Wofsy, S. C., Kort, E. A., Sweeney, C., Schuck, T., Brenninkmeijer, C., Chen, H., Beck, V., and Gerbig, C.: Atmospheric CH_4 in the first decade of the 21st century: Inverse modeling analysis using SCIAMACHY satellite retrievals and NOAA surface measurements, J. Geophys. Res. Atmos., 118, 7350–7369, https://doi.org/10.1002/jgrd.50480, 2013.

Bergamaschi, P., Segers, A., Brunner, D., Haussaire, J.-M., Henne, S., Ramonet, M., Arnold, T., Biermann, T., Chen, H., Conil, S., Delmotte, M., Forster, G., Frumau, A., Kubistin, D., Lan, X., Leuenberger, M., Lindauer, M., Lopez, M., Manca, G., Müller-Williams, J., O'Doherty, S., Scheeren, B., Steinbacher, M., Trisolino, P., Vítková, G., and Yver Kwok, C.: High-resolution inverse modelling of European CH_4 emissions using the novel FLEXPART-COSMO TM5 4DVAR inverse modelling system, Atmos. Chem. Phys., 22, 13 243–13 268, https://doi.org/10.5194/acp-22-13243-2022, 2022.

Bisht, J. S. H., Patra, P. K., Takigawa, M., Sekiya, T., Kanaya, Y., Saitoh, N., and Miyazaki, K.: Estimation of CH_4 emission based on an advanced 4D-LETKF assimilation system, Geoscientific Model Development, 16, 1823–1838, https://doi.org/10.5194/gmd-16-1823-2023, 2023.

Bloom, A., Bowman, K., Lee, M., Turner, A., Schroeder, R., Worden, J., Weidner, R., McDonald, K., and Jacob, D.: CMS: Global 0.5-deg Wetland Methane Emissions and Uncertainty (WetCHARTs v1.3.1), https://doi.org/10.3334/ORNLDAAC/2346, 2024.

Bruch, V., Rösch, T., Jiménez de la Cuesta Otero, D., Ellerhoff, B., Mamtimin, B., Becker, N., Blechschmidt, A.-M., Förstner, J., and Kaiser-Weiss, A. K.: German methane fluxes estimated top-down using ICON–ART – Part 1: Ensemble-enhanced scaling inversion, Atmospheric Chemistry and Physics, 25, 17 159–17 185, https://doi.org/10.5194/acp-25-17159-2025, 2025a.

Bruch, V., Rösch, T., Jiménez de la Cuesta Otero, D., Ellerhoff, B., Mamtimin, B., Becker, N., Blechschmidt, A.-M., Förstner, J., and Kaiser-Weiss, A. K.: German methane fluxes estimated top-down using ICON–ART – Part 2: Inversion results for 2021, Atmospheric Chemistry and Physics, 25, 17 187–17 204, https://doi.org/10.5194/acp-25-17187-2025, 2025b.

Bruch, V., Rösch, T., Steil, M. J., Jiménez de la Cuesta Otero, D., Ellerhoff, B., Becker, N., Böttcher, J., Blechschmidt, A.-M., Mamtimin, B., and Kaiser-Weiss, A. K.: European methane emissions estimated top-down with the ITMS demonstrator v2025, https://doi.org/10.5281/zenodo.20429765, 2026.

Chen, H. W., Zhang, F., Lauvaux, T., Davis, K. J., Feng, S., Butler, M. P., and Alley, R. B.: Characterization of Regional-Scale CO_2 Transport Uncertainties in an Ensemble with Flow-Dependent Transport Errors, Geophys. Res. Lett., 46, 4049–4058, https://doi.org/10.1029/2018GL081341, 2019.

Deng, Z., Ciais, P., Tzompa-Sosa, Z. A., Saunois, M., Qiu, C., Tan, C., Sun, T., Ke, P., Cui, Y., Tanaka, K., Lin, X., Thompson, R. L., Tian, H., Yao, Y., Huang, Y., Lauerwald, R., Jain, A. K., Xu, X., Bastos, A., Sitch, S., Palmer, P. I., Lauvaux, T., D'Aspremont, A., Giron, C., Benoit, A., Poulter, B., Chang, J., Petrescu, A. M. R., Davis, S. J., Liu, Z., Grassi, G., Albergel, C., Tubiello, F. N., Perugini, L., Peters, W., and Chevallier, F.: Comparing national greenhouse gas budgets reported in UNFCCC inventories against atmospheric inversions, Earth Syst. Sci. Data, 14, 1639–1675, https://doi.org/10.5194/essd-14-1639-2022, 2022.

East, J. D., Jacob, D. J., Jervis, D., Balasus, N., Estrada, L. A., Hancock, S. E., Sulprizio, M. P., Thomas, J., Wang, X., Chen, Z., Varon, D. J., and Worden, J. R.: Worldwide inference of national methane emissions by inversion of satellite observations with UNFCCC prior estimates, Nature Communications, 16, https://doi.org/10.1038/s41467-025-67122-8, 2025.

Engelen, R. J., Denning, A. S., and Gurney, K. R.: On error estimation in atmospheric CO_2 inversions, J. Geophys. Res. Atmos., 107, ACL10–1–ACL10–13, https://doi.org/10.1029/2002JD002195, 2002.

Enting, I. G.: Inverse problems in atmospheric constituent studies: III. Estimating errors in surface sources, Inverse Problems, 9, 649, https://doi.org/10.1088/0266-5611/9/6/004, 1993.

Estrada, L. A., Varon, D. J., Sulprizio, M., Nesser, H., Chen, Z., Balasus, N., Hancock, S. E., He, M., East, J. D., Mooring, T. A., Oort Alonso, A., Maasakkers, J. D., Aben, I., Baray, S., Bowman, K. W., Worden, J. R., Cardoso-Saldaña, F. J., Reidy, E., and Jacob, D. J.: Integrated Methane Inversion (IMI) 2.0: an improved research and stakeholder tool for monitoring total methane emissions with high resolution worldwide using TROPOMI satellite observations, EGUsphere [preprint], pp. 1–31, https://doi.org/10.5194/egusphere-2024-2700, 2024.

European Commission: Launch by United States, the European Union, and Partners of the Global Methane Pledge to Keep 1.5C Within Reach, https://ec.europa.eu/commission/presscorner/detail/en/statement_21_5766, (last accessed: 19 January 2026), 2021.

Evensen, G.: Sequential data assimilation with a nonlinear quasi-geostrophic model using Monte Carlo methods to forecast error statistics, Journal of Geophysical Research: Oceans, 99, 10 143–10 162, https://doi.org/https://doi.org/10.1029/94JC00572, 1994.

Feigenspan, S. and Wernicke, T.: Personal communication, 2025.

Ganesan, A. and Manning, A.: GAW Report No. 319: Integrated Global Greenhouse Gas Information System Good Practice Guidance for Estimating National-scale Greenhouse Gas Emissions using Atmospheric Observations, https://library.wmo.int/idurl/4/69714, 2025.

Ganesan, A., Manning, A., Henne, S., De Longueville, H., Ramsden, A., Brito Melo, D., Danjou, A., Andrews, P., Murphy, B., Redington, A., and Pitt, J.: Inverse modelling results for European non-CO2 greenhouse gas emissions, https://doi.org/10.18160/GR1Q-6SK4, 2026.

Ganesan, A. L., Manning, A. J., Grant, A., Young, D., Oram, D. E., Sturges, W. T., Moncrieff, J. B., and O'Doherty, S.: Quantifying methane and nitrous oxide emissions from the UK and Ireland using a national-scale monitoring network, Atmos. Chem. Phys., 15, 6393–6406, https://doi.org/10.5194/acp-15-6393-2015, 2015.

Gaspari, G. and Cohn, S. E.: Construction of correlation functions in two and three dimensions, Quarterly Journal of the Royal Meteorological Society, 125, 723–757, https://doi.org/https://doi.org/10.1002/qj.49712555417, 1999.

Gerbig, C., Körner, S., and Lin, J. C.: Vertical mixing in atmospheric tracer transport models: error characterization and propagation, Atmos. Chem. Phys., 8, 591–602, https://doi.org/10.5194/acp-8-591-2008, 2008.

Gilpin, S.: Inaccuracy of Ensemble-Based Covariance Propagation, Beyond Sampling Error, https://arxiv.org/abs/2508.16567, 2025.

Gilpin, S., Matsuo, T., and Cohn, S. E.: Inaccuracy of the variance evolution associated with discrete covariance propagation, Quarterly Journal of the Royal Meteorological Society, 151, e5016, https://doi.org/https://doi.org/10.1002/qj.5016, 2025.

Henne, S., Brunner, D., Oney, B., Leuenberger, M., Eugster, W., Bamberger, I., Meinhardt, F., Steinbacher, M., and Emmenegger, L.: Validation of the Swiss methane emission inventory by atmospheric observations and inverse modelling, Atmos. Chem. Phys., 16, 3683–3710, https://doi.org/10.5194/acp-16-3683-2016, 2016.

Hunt, B. R., Kostelich, E. J., and Szunyogh, I.: Efficient data assimilation for spatiotemporal chaos: A local ensemble transform Kalman filter, Physica D, 230, 112–126, https://doi.org/10.1016/j.physd.2006.11.008, 2007.

ICOS RI: ICOS Handbook 2024, https://doi.org/10.18160/28AV-80QR, 2024.

ICOS RI, Bergamaschi, P., Colomb, A., De Mazière, M., Emmenegger, L., Kubistin, D., Lehner, I., Lehtinen, K., Leuenberger, M., Lund Myhre, C., Marek, M. V., O'Doherty, S., Platt, S. M., Plaß-Dülmer, C., Apadula, F., Arnold, S., Blanc, P.-E., Brunner, D., Chen, H., Chmura, L., Chmura, Ł., Conil, S., Couret, C., Cristofanelli, P., Forster, G., Frumau, A., Gerbig, C., Gheusi, F., Hammer, S., Haszpra, L., Hatakka, J., Heliasz, M., Henne, S., Hensen, A., Hoheisel, A., Kneuer, T., Larmanou, E., Laurila, T., Leskinen, A., Levin, I., Lindauer, M., Lopez, M., Mammarella, I., Manca, G., Manning, A., Martin, D., Meinhardt, F., Mölder, M., Müller-Williams, J., Noe, S. M., Nęcki, J., Ottosson-Löfvenius, M., Philippon, C., Pitt, J., Ramonet, M., Rivas-Soriano, P., Scheeren, B., Schumacher, M., Sha, M. K., Spain, G., Steinbacher, M., Sørensen, L. L., Vermeulen, A., Vítková, G., Xueref-Remy, I., di Sarra, A., Conen, F., Kazan, V., Roulet, Y.-A., Biermann, T., Delmotte, M., Heltai, D., Hermansen, O., Komínková, K., Laurent, O., Levula, J., Lunder, C., Marklund, P., Morguí, J.-A., Pichon, J.-M., Schmidt, M., Sferlazzo, D., Smith, P., Stanley, K., Trisolino, P., Zazzeri, G., ICOS Carbon Portal, ICOS Atmosphere Thematic Centre, ICOS Flask And Calibration Laboratory, and ICOS Central Radiocarbon Laboratory: European Obspack compilation of atmospheric methane data from ICOS and non-ICOS European stations for the period 1984–2024; `obspack_ch4_466_GVeu_v9.2_20240502`, https://doi.org/10.18160/9B66-SQM1, 2024.

Ioannidis, E., Meesters, A., Steiner, M., Brunner, D., Reum, F., Pison, I., Berchet, A., Thompson, R., Sollum, E., Koch, F.-T., Gerbig, C., Wang, F., Maksyutov, S., Tsuruta, A., Tenkanen, M., Aalto, T., Monteil, G., Lin, H., Ren, G., Scholze, M., and Houweling, S.: An intercomparison of inverse models for estimating European CH_4 emissions, Earth Syst. Sci. Data, 18, 167–198, https://doi.org/10.5194/essd-18-167-2026, 2026.

IPCC, Calvo Buendia, E., Tanabe, K., Kranjc, A., Baasansuren, J., Fukuda, M., Ngarize, S., Osako, A., Pyrozhenko, Y., Shermanau, P., and Federici, S., eds.: 2019 Refinement to the 2006 IPCC Guidelines for National Greenhouse Gas Inventories, vol. 1, The Intergovernmental Panel on Climate Change (IPCC), https://www.ipcc-nggip.iges.or.jp/public/2019rf/index.html, 2019.

Jähn, M., Kuhlmann, G., Mu, Q., Haussaire, J.-M., Ochsner, D., Osterried, K., Clément, V., and Brunner, D.: An online emission module for atmospheric chemistry transport models: implementation in COSMO-GHG v5.6a and COSMO-ART v5.1-3.1, Geosci. Model Dev., 13, 2379–2392, https://doi.org/10.5194/gmd-13-2379-2020, 2020.

Kaminski, T., Rayner, P. J., Heimann, M., and Enting, I. G.: On aggregation errors in atmospheric transport inversions, J. Geophys. Res. Atmos., 106, 4703–4715, https://doi.org/10.1029/2000JD900581, 2001.

Kuenen, J., Dellaert, S., Visschedijk, A., Jalkanen, J.-P., Super, I., and Denier van der Gon, H.: Copernicus Atmosphere Monitoring Service regional emissions version 4.2 (CAMS-REG-v4.2), Copernicus Atmosphere Monitoring Service (CAMS) [publisher], ECCAD [distributor], https://doi.org/10.24380/0vzb-a387, 2021a.

Kuenen, J., Dellaert, S., Visschedijk, A., Jalkanen, J.-P., Super, I., and Denier van der Gon, H.: Copernicus Atmosphere Monitoring Service regional emissions version 5.1 business-as-usual 2020 (CAMS-REG-v5.1 BAU 2020), https://doi.org/10.24380/eptm-kn40, 2021b.

Kuenen, J., Dellaert, S., Visschedijk, A., Jalkanen, J.-P., Super, I., and Denier van der Gon, H.: CAMS-REG-v4: a state-of-the-art high-resolution European emission inventory for air quality modelling, Earth Syst. Sci. Data, 14, 491–515, https://doi.org/10.5194/essd-14-491-2022, 2022.

Le Dimet, F.-X. and Talagrand, O.: Variational algorithms for analysis and assimilation of meteorological observations: theoretical aspects, Tellus, 38, 97–110, https://doi.org/10.3402/tellusa.v38i2.11706, 1986.

Logan, J. A., Prather, M. J., Wofsy, S. C., and McElroy, M. B.: Tropospheric chemistry: A global perspective, Journal of Geophysical Research: Oceans, 86, 7210–7254, https://doi.org/https://doi.org/10.1029/JC086iC08p07210, 1981.

Malardel, S., Diamantakis, M., Panareda, A., and Flemming, J.: Dry mass versus total mass conservation in the IFS, ECMWF Technical Memoranda 849, ECMWF, https://doi.org/10.21957/s3ho2aq29, 2019.

https://doi.org/10.5194/egusphere-2026-3221
Preprint. Discussion started: 7 August 2026

Manning, A., Ganesan, A., de Longueville, H., Danjou, A., Murphy, B., Henne, S., Melo, D. B., Ramsden, A., Redington, A., and Andrews, P.: Draft annex to National Inventory Report (NIR) for each focus country – first update, PARIS - Process Attribution of Regional Emissions, https://horizoneurope-paris.eu/wp-content/uploads/sites/914/2026/01/PARIS-D2.3-Draft-Annexes-to-National-Inventory-Reports-1st-update-final-complete-reduced.pdf, (last accessed: 12 February 2026), 2025.

Manning, A. J., O'Doherty, S., Jones, A. R., Simmonds, P. G., and Derwent, R. G.: Estimating UK methane and nitrous oxide emissions from 1990 to 2007 using an inversion modeling approach, J. Geophys. Res. Atmos., 116, https://doi.org/10.1029/2010JD014763, 2011.

Meirink, J. F., Bergamaschi, P., and Krol, M. C.: Four-dimensional variational data assimilation for inverse modelling of atmospheric methane emissions: method and comparison with synthesis inversion, Atmos. Chem. Phys., 8, 6341–6353, https://doi.org/10.5194/acp-8-6341-2008, 2008.

Miyazaki, K., Eskes, H. J., Sudo, K., Takigawa, M., van Weele, M., and Boersma, K. F.: Simultaneous assimilation of satellite NO_2, O_3, CO, and HNO_3 data for the analysis of tropospheric chemical composition and emissions, Atmospheric Chemistry and Physics, 12, 9545–9579, https://doi.org/10.5194/acp-12-9545-2012, 2012.

Munassar, S., Monteil, G., Scholze, M., Karstens, U., Rödenbeck, C., Koch, F.-T., Totsche, K. U., and Gerbig, C.: Why do inverse models disagree? A case study with two European CO_2 inversions, Atmos. Chem. Phys., 23, 2813–2828, https://doi.org/10.5194/acp-23-2813-2023, 2023.

Nakamura, G. and Potthast, R.: Inverse Modeling – An introduction to the theory and methods of inverse problems and data assimilation, IOP Publishing, Bristol, England, UK, ISBN 978-0-7503-1218-9, https://doi.org/10.1088/978-0-7503-1218-9, 2015.

Peng, Z., Liu, Z., Chen, D., and Ban, J.: Improving $PM_{2.5}$ forecast over China by the joint adjustment of initial conditions and source emissions with an ensemble Kalman filter, Atmospheric Chemistry and Physics, 17, 4837–4855, https://doi.org/10.5194/acp-17-4837-2017, 2017.

Petrescu, A. M. R., Qiu, C., McGrath, M. J., Peylin, P., Peters, G. P., Ciais, P., Thompson, R. L., Tsuruta, A., Brunner, D., Kuhnert, M., Matthews, B., Palmer, P. I., Tarasova, O., Regnier, P., Lauerwald, R., Bastviken, D., Höglund-Isaksson, L., Winiwarter, W., Etiope, G., Aalto, T., Balsamo, G., Bastrikov, V., Berchet, A., Brockmann, P., Ciotoli, G., Conchedda, G., Crippa, M., Dentener, F., Groot Zwaaftink, C. D., Guizzardi, D., Günther, D., Haussaire, J.-M., Houweling, S., Janssens-Maenhout, G., Kouyate, M., Leip, A., Leppänen, A., Lugato, E., Maisonnier, M., Manning, A. J., Markkanen, T., McNorton, J., Muntean, M., Oreggioni, G. D., Patra, P. K., Perugini, L., Pison, I., Raivonen, M. T., Saunois, M., Segers, A. J., Smith, P., Solazzo, E., Tian, H., Tubiello, F. N., Vesala, T., van der Werf, G. R., Wilson, C., and Zaehle, S.: The consolidated European synthesis of CH_4 and N_2O emissions for the European Union and United Kingdom: 1990–2019, Earth Syst. Sci. Data, 15, 1197–1268, https://doi.org/10.5194/essd-15-1197-2023, 2023.

Petrescu, A. M. R., Peters, G. P., Engelen, R., Houweling, S., Brunner, D., Tsuruta, A., Matthews, B., Patra, P. K., Belikov, D., Thompson, R. L., Höglund-Isaksson, L., Zhang, W., Segers, A. J., Etiope, G., Ciotoli, G., Peylin, P., Chevallier, F., Aalto, T., Andrew, R. M., Bastviken, D., Berchet, A., Broquet, G., Conchedda, G., Dellaert, S. N. C., Denier van der Gon, H., Gütschow, J., Haussaire, J.-M., Lauerwald, R., Markkanen, T., van Peet, J. C. A., Pison, I., Regnier, P., Solum, E., Scholze, M., Tenkanen, M., Tubiello, F. N., van der Werf, G. R., and Worden, J. R.: Comparison of observation- and inventory-based methane emissions for eight large global emitters, Earth Syst. Sci. Data, 16, 4325–4350, https://doi.org/10.5194/essd-16-4325-2024, 2024.

Prill, F., Reinert, D., Rieger, D., and Zängl, G.: ICON Tutorial 2024, Deutscher Wetterdienst, https://doi.org/10.5676/DWD_pub/nwv/icon_tutorial2024, 2024.

Ramsden, A., Danjou, A., Longueville, H. D., Melo, D., Constantin, L., Thanwerdas, J., Henne, S., Bruch, V., Maier, F., and Herrfurth, L.: Flux Intercomparison Environment Fluxie v2.0., https://github.com/openghg/fluxie, (last accessed: 7 April 2026), 2026.

Rieger, D., Bangert, M., Bischoff-Gauss, I., Förstner, J., Lundgren, K., Reinert, D., Schröter, J., Vogel, H., Zängl, G., Ruhnke, R., and Vogel, B.: ICON–ART 1.0 – a new online-coupled model system from the global to regional scale, Geosci. Model Dev., 8, 1659–1676, https://doi.org/10.5194/gmd-8-1659-2015, 2015.

Rocher-Ros, G., Stanley, E. H., Loken, L. C., Casson, N. J., Raymond, P. A., Liu, S., Amatulli, G., and Sponseller, R. A.: Global methane emissions from rivers and streams, Nature, 621, 530–535, https://doi.org/10.1038/s41586-023-06344-6, 2023.

Schraff, C., Reich, H., Rhodin, A., Schomburg, A., Stephan, K., Periáñez, A., and Potthast, R.: Kilometre-scale ensemble data assimilation for the COSMO model (KENDA), Q. J. R. Meteorolog. Soc., 142, 1453–1472, https://doi.org/10.1002/qj.2748, 2016.

Schröter, J., Rieger, D., Stassen, C., Vogel, H., Weimer, M., Werchner, S., Förstner, J., Prill, F., Reinert, D., Zängl, G., Giorgetta, M., Ruhnke, R., Vogel, B., and Braesicke, P.: ICON-ART 2.1: a flexible tracer framework and its application for composition studies in numerical weather forecasting and climate simulations, Geosci. Model Dev., 11, 4043–4068, https://doi.org/10.5194/gmd-11-4043-2018, 2018.

Segers, A. and Houweling, S.: CAMS global inversion-optimised greenhouse gas fluxes and concentrations, v24r1, Copernicus Atmosphere Monitoring Service [data set], https://ads.atmosphere.copernicus.eu/datasets/cams-global-greenhouse-gas-inversion, (last accessed: 1 December 2025), 2020.

Shindell, D., Kuylenstierna, J. C. I., Vignati, E., van Dingenen, R., Amann, M., Klimont, Z., Anenberg, S. C., Muller, N., Janssens-Maenhout, G., Raes, F., Schwartz, J., Faluvegi, G., Pozzoli, L., Kupiainen, K., Höglund-Isaksson, L., Emberson, L., Streets, D., Ramanathan, V., Hicks, K., Oanh, N. T. K., Milly, G., Williams, M., Demkine, V., and Fowler, D.: Simultaneously Mitigating Near-Term Climate Change and Improving Human Health and Food Security, Science, 335, 183–189, https://doi.org/10.1126/science.1210026, 2012.

Steiner, M., Cantarello, L., Henne, S., and Brunner, D.: Flow-dependent observation errors for greenhouse gas inversions in an ensemble Kalman smoother, Atmos. Chem. Phys., 24, 12 447–12 463, https://doi.org/10.5194/acp-24-12447-2024, 2024a.

Steiner, M., Peters, W., Luijkx, I., Henne, S., Chen, H., Hammer, S., and Brunner, D.: European CH_4 inversions with ICON-ART coupled to the CarbonTracker Data Assimilation Shell, Atmos. Chem. Phys., 24, 2759–2782, https://doi.org/10.5194/acp-24-2759-2024, 2024b.

Stern, N.: The Growth Story of the 21st Century: The Economics and Opportunity of Climate Action, LSE Press, 10 Portugal Street, London, UK, ISBN 978-1-911712-48-0, https://doi.org/https://doi.org/10.31389/lsepress.tgs, 2025.

Stohl, A., Seibert, P., Arduini, J., Eckhardt, S., Fraser, P., Greally, B. R., Lunder, C., Maione, M., Mühle, J., O'Doherty, S., Prinn, R. G., Reimann, S., Saito, T., Schmidbauer, N., Simmonds, P. G., Vollmer, M. K., Weiss, R. F., and Yokouchi, Y.: An analytical inversion method for determining regional and global emissions of greenhouse gases: Sensitivity studies and application to halocarbons, Atmos. Chem. Phys., 9, 1597–1620, https://doi.org/10.5194/acp-9-1597-2009, 2009.

Storm, I., Karstens, U., D'Onofrio, C., Vermeulen, A., and Peters, W.: A view of the European carbon flux landscape through the lens of the ICOS atmospheric observation network, Atmos. Chem. Phys., 23, 4993–5008, https://doi.org/10.5194/acp-23-4993-2023, 2023.

UBA: Submission under the United Nations Framework Convention on Climate Change 2025, German Environment Agency, https://unfccc.int/documents/646518, 2025.

Valmassoi, A., Anlauf, H., Becker, A., Keller, J. D., Krebber, S., Zängl, G., Potthast, R., Cress, A., Fundel, F., Hanisch, T., Lange, M., Steinert, T., and Kaspar, F.: ICON-DREAM: ICON-Dual resolution Reanalysis for Emulators, Applications and Monitoring The ICON-Dual resolution reanalysis version v1.0., Deutscher Wetterdienst, https://doi.org/10.5676/dwd/icon-dream_v1, 2025.

van der Net, L., Coenen, P., van Mil, S., Rienstra, J., Zijlema, P., Baas, K., van Baren, S., Dröge, R., Geertjes, K., Honig, E., van Huet, B., te Molder, R., Montfoort, J., van der Zee, T., Witt, H., and van Zanten, M.: Greenhouse gas emissions in the Netherlands 1990-2023. National Inventory Document 2025, National Institute for Public Health and the Environment (RIVM), https://doi.org/10.21945/RIVM-2025-0005, 2025.

https://doi.org/10.5194/egusphere-2026-3221
Preprint. Discussion started: 7 August 2026

Weber, T., Wiseman, N. A., and Kock, A.: Global ocean methane emissions dominated by shallow coastal waters, Nat. Commun., 10, 1–10, https://doi.org/10.1038/s41467-019-12541-7, 2019.

Wecht, K. J., Jacob, D. J., Frankenberg, C., Jiang, Z., and Blake, D. R.: Mapping of North American methane emissions with high spatial resolution by inversion of SCIAMACHY satellite data, Journal of Geophysical Research: Atmospheres, 119, 7741–7756, https://doi.org/https://doi.org/10.1002/2014JD021551, 2014.

West, D. H. D.: Updating mean and variance estimates: an improved method, Commun. ACM, 22, 532–535, https://doi.org/10.1145/359146.359153, 1979.

Witt, H.: Personal communication, 2025.

Zängl, G., Reinert, D., Rípodas, P., and Baldauf, M.: The ICON (ICOsahedral Non-hydrostatic) modelling framework of DWD and MPI-M: Description of the non-hydrostatic dynamical core, Quart. J. Roy. Meteorol. Soc., 141, 563–579, https://doi.org/10.1002/qj.2378, 2015.